Loss of Bbs8 leads to cystic kidney disease in mice with reduced acetylation of ciliary alpha-tubulin through HDAC2

Emilia Kieckhöfer[1,2], Julia Günzler[1,2,#], Peter A. Matthiessen[3,#], Lena K. Ebert[1,2], Christina Klausen[4], Dagmar Wachten[4], Metin Cetiner[5], Max C. Liebau[6], Thomas Benzing[1,2], Helen May-Simera[3,*], Bernhard Schermer[1,2,*,§]

[1] *Department II of Internal Medicine and Center for Molecular Medicine Cologne, University of Cologne, Faculty of Medicine and University Hospital Cologne, Cologne, Germany.*

[2] *Cologne Excellence Cluster on Cellular Stress Responses in Aging-Associated Diseases (CECAD), University of Cologne, Faculty of Medicine and University Hospital Cologne, Cologne, Germany.*

[3] *Faculty of Biology, Ciliary Cell Biology, Institute of Molecular Physiology, Johannes Gutenberg-University, Mainz, Germany.*

[4] *Institute of Innate Immunity, Biophysical Imaging, Medical Faculty, University of Bonn, Bonn, Germany.*

[5] *Department of Pediatric Nephrology, Pediatrics II, University of Duisburg-Essen, Essen, Germany.*

[6] *Department of Pediatrics and Center for Molecular Medicine Cologne, University Hospital Cologne and Faculty of Medicine, University of Cologne, Cologne, Germany.*

 # These authors contributed equally.

**** These authors contributed equally.***

[§]***corresponding author:*** bernhard.schermer@uk-koeln.de

Keywords: BBS, primary cilium, kidney, ciliopathies, cysts, HDAC2

Abstract

Primary cilia dysfunction underlies a group of severe disorders known as ciliopathies. These include Bardet-Biedl syndrome (BBS), which is caused by mutations in BBS genes encoding for components of ciliary protein complexes essential for the assembly and maintenance of primary cilia. As in most ciliopathies, a hallmark feature of BBS is the development of cystic kidney disease. However, the molecular mechanisms linking ciliary dysfunction to cystogenesis remain incompletely understood. Here, we show that *Bbs8*$^{-/-}$ mice develop late-onset cystic kidney disease accompanied by increased regulated cell death and fibrosis. While the number and length of cilia are not affected, loss of BBS8 reduces K40 acetylation of α-tubulin within primary cilia, compromising ciliary stability. Notably, proteomic analysis revealed a significant upregulation of histone deacetylase HDAC2 in *Bbs8*$^{-/-}$ kidneys, which we confirmed in *Bbs8*$^{-/-}$ mouse embryonic fibroblasts (MEFs) and in urine-derived renal epithelial cells (URECs) from a BBS8 patient. We further demonstrate the protein interaction between BBS8 and HDAC2, implicating a disrupted BBS8–HDAC2 regulatory axis in disease pathogenesis. Consistent with a role of excessive HDAC2 activity in the BBS8 deficient cells, pharmacological inhibition of HDAC2 restored tubulin acetylation in BBS8 urine-derived cells. Thus, modulation of HDAC2 activity may represent a strategy to alter ciliary stability *in vivo* which could explain positive effects of class I specific HDAC inhibitors in models of cystic kidney disease.

Introduction

The primary cilium is a specialized microtubule-based sensory organelle extending from most mammalian cells' surfaces (Pazour and Bloodgood, 2008). It consists of the axoneme, ensheathed by the ciliary membrane, the transition zone, and the basal body, which anchors the cilium to the cell body. The transition zone between the basal body and the ciliary shaft is critical for protein trafficking to and from the ciliary compartment (Reiter, Blacque and Leroux, 2012; Garcia-Gonzalo and Reiter, 2017). Tight regulation of the protein composition is required for cilia to function as a hub for chemo- and mechano-transduction, as well as ciliary signaling (Reiter, Blacque and Leroux, 2012). As such, they play a pivotal role in modulating various signaling pathways, e.g. Hedgehog, Wnt, and TGF-β signaling (Fan and Tessier-Lavigne, 1994; Munsterberg *et al.*, 1995; Pourquié *et al.*, 1996). Unlike any other organelle, cilia periodically disappear during the mitotic cell cycle: When cells re-enter mitosis, cilia are typically

29 disassembled to subsequently release the basal body, a modified mother centriole, to serve as
30 microtubule organizing centers at the spindle poles. Disassembly of cilia mechanistically involves the
31 deacetylation of ciliary α-tubulin by HDAC6 and, thus, destabilization of microtubules (Pugacheva *et al.*,
32 2007; Gopalakrishnan *et al.*, 2023). It is well established that pathogenetic variants in proteins, which
33 alter the structure or function of cilia, lead to a heterogeneous group of genetic diseases and syndromes
34 referred to as ciliopathies (Hildebrandt, Benzing and Katsanis, 2011). Ciliopathies comprise a diverse
35 group of genetic disorders with overlapping phenotypes in different organs and tissues, such as the
36 brain, eye, skeleton, liver, vasculature, and kidney (Forsythe and Beales, 2013; Reiter and Leroux, 2017).
37 Thereby, cystic and fibrotic kidney diseases are a common occurrence among many ciliopathies, leading
38 to the frequent classification of a significant subgroup, namely: renal ciliopathies (Hildebrandt and Zhou,
39 2007; McConnachie, Stow and Mallett, 2021).

40 The Bardet-Biedl Syndrome is an archetypical autosomal-recessive ciliopathy characterized by obesity,
41 retinopathy, polydactyly, and kidney disease (Forsythe and Beales, 2013). This syndrome is caused by
42 pathogenic variants of BBS genes encoding for BBS proteins. Most BBS proteins can be classified
43 according to the particular protein complexes which they form. The BBSome complex (Nachury *et al.*,
44 2007; Loktev *et al.*, 2008) (BBS1, BBS2, BBS4, BBS5, BBS7, BBS8, BBS9, BBS18) is required for trafficking of
45 ciliary membrane proteins whereas, the chaperonin-like complex (BBS6, BBS10, and BBS12), catalyzes
46 the assembly of the BBSome (Seo *et al.*, 2010). The remaining BBS proteins have varying specific
47 functions but are predicted to influence ciliary trafficking. The kidney phenotype in BBS patients is
48 variable with kidneys showing parenchymal, medullary, and most often corticomedullary cysts, but also
49 renal fibrosis, unilateral agenesis, or dysplastic kidneys (Beales *et al.*, 1999; Putoux *et al.*, 2012; Forsythe
50 *et al.*, 2017; Elawad *et al.*, 2022). However, these phenotypes are highly variable among families and
51 could be dependent on mutation type (Putoux *et al.*, 2012; Forsythe *et al.*, 2017).

52 Studies on various *Bbs* mutant mice, including *Bbs1*^{M390R} transgenic, *Bbs2*$^{-/-}$, *Bbs4*$^{-/-}$, *Bbs5*$^{-/-}$, *Bbs6*$^{-/-}$, *Bbs8*$^{-/-}$
53 and *Bbs10*$^{-/-}$, revealed significant parallels to human disease. These mice exhibit a broad spectrum of
54 vision impairment, obesity, male infertility, and neurological deficits (Kulaga *et al.*, 2004; Mykytyn *et al.*,
55 2004; Nishimura *et al.*, 2004; Fath *et al.*, 2005; Davis *et al.*, 2007; Rahmouni *et al.*, 2008; Seo *et al.*, 2009;
56 Cognard *et al.*, 2015; Kretschmer *et al.*, 2019; Bentley-Ford *et al.*, 2021; Rödig *et al.*, 2022; Sieckmann *et*
57 *al.*, 2024). For BBS10, complete knockout resulted in renal abnormalities primarily affecting glomeruli
58 and podocytes without cyst formation, while a tubular epithelial cell-specific knockout did not show any
59 overt phenotype (Cognard *et al.*, 2015). Cyst formation has been observed in *Bbs2*$^{-/-}$ and *Bbs4*$^{-/-}$ mice, but
60 again primarily affecting glomeruli (Nishimura *et al.*, 2004; Guo *et al.*, 2011). Loss of *Bbs8* has so far

61 shown to cause the most severe retinal phenotype in mice (Tadenev *et al.*, 2011; Dilan *et al.*, 2018;
62 Kretschmer *et al.*, 2019; Schneider *et al.*, 2021), which is not only caused by ciliary defects of
63 photoreceptor cells but also due to ciliary defects in the retinal pigment epithelium (RPE) (Kretschmer *et*
64 *al.*, 2023; Schneider *et al.*, 2021). BBS8 is one of the key components of the BBSome, which might explain
65 the severity of the *Bbs8*$^{-/-}$ phenotype. BBS8 (TTC8) is a tetratricopeptide repeat (TPR) protein with a
66 critical role in planar cell polarity and laterality (May-Simera *et al.*, 2010, 2015; Patnaik *et al.*, 2019). Loss
67 of *Bbs8* leads to changes in the composition of the octameric BBSome complex, where BBS8 is a direct
68 interactor of the scaffold protein BBS9 (Zhang *et al.*, 2012).

69 Until now, research into BBS8 function has predominantly focused on embryonic development and
70 ocular health. A subtle renal phenotype, characterized by mild tubular dilation at around 8 months of
71 age, has been reported (Tadenev *et al.*, 2011), but specific roles of BBS8 in maintaining renal cilia and
72 preserving kidney architecture remain largely unexplored. In this study, we report the occurrence of
73 tubular cystic kidney disease in *Bbs8*-deficient mice at 46 weeks of age, accompanied by renal fibrosis
74 and increased rate of regulated cell death. Interestingly, neither cilia number, nor length differed
75 significantly from wild-type littermates; however, the levels of acetylated tubulin within primary cilia
76 were markedly reduced. We demonstrate that this reduction, which destabilizes cilia, is driven by
77 increased expression of histone deacetylase HDAC2. This effect is confirmed in isolated mouse
78 embryonic fibroblasts (MEFs) and urine-derived renal epithelial cells (URECs) from a BBS8 patient. Thus,
79 beyond potential therapeutic implications of HDAC2 inhibition, our data highlight the importance of not
80 relying solely on acetylated tubulin as a marker for cilia in functional studies, particularly in disease
81 contexts where ciliary stability is affected.

82 **Methods**

83 *Mouse lines*

84 *Bbs8*$^{-/-}$ mice have been previously described (Tadenev *et al.*, 2011). All animals were housed, handled,
85 and animal studies conducted, in accordance with approved institutional animal care and use committee
86 procedures. All experiments had ethical approval from the Landesuntersuchungsamt Rheinland-Pfalz and
87 were performed in accordance with institutional guidelines for animal welfare, German animal
88 protection law, and the guidelines given by the ARVO Statement for the Use of Animals in Ophthalmic
89 and Vision Research. Animal maintenance and handling were performed in line with the Federation for
90 Laboratory Animal Science Associations (FELASA) recommendations. Animals were housed in a 12 h
91 light/dark cycle with food and water available *ad libitum*. For the preparation, mice were weighted,

92 followed by cervical dislocation; blood was collected prior to the perfusion of the kidney with PBS
93 through the aorta. Further, other organs and fat tissue were taken and, as the kidney, processed by
94 either fixation in 4 % formaldehyde and embedded in paraffin or snap-frozen for further tissue analysis.
95 The blood was incubated for 2 h at RT, followed by centrifugation. Serum creatinine levels were
96 measured by the Institute of Clinical Chemistry, University Hospital of Cologne, Germany.

97 *Immunohistology*

98 For histological analysis, tissue was cut into 2-µm-thick sections and deparaffinized by xylene treatment
99 and rehydration in graded ethanol. For PAS staining, the sections were stained with 0,9 % periodic acid
100 (cat# 3257.1, Roth) and Schiffsches Reagent (cat# 1.09033, Merck) both for 10 min embedded into
101 washing steps with H_2O. Finally, to visualize nuclei in blue, the samples were stained with Mayer's
102 Haematoxylin for 20 s. For the Masson staining the Masson-Goldner's trichrome staining kit (cat# 3459,
103 Roth) was used and performed according to the manufacturer's instructions. After dehydration of the
104 sections, they were embedded with Histomount (HS-103, National Diagnostics).

105 *Cyst index analysis*

106 The cyst index was calculated for whole slide images using open-source software for bioimage analysis
107 QuPath (v0.4.0) (Bankhead *et al.*, 2017). Cysts were detected using an Artificial Neural Network-based
108 pixel classifier. Initially detected cysts were filtered for the minimal area of 400 μm^2 and a minimum
109 circularity value of 0.35. Plots were generated using the Plots of Data web app (Postma and Goedhartid,
110 2019). For statistical analysis, all results were normalized to the control followed by a two-tailed
111 Student's *t*-test ($p<0.05$).

112 *Proteome and phosphoproteome analysis*

113 For each biological replicate a quarter of kidney tissue was used and dounced with a Wheaton Dounce
114 tissue grinder in urea buffer (8 M Urea, 50 mM ammonium bicarbonate) supplemented with Halt
115 protease-phosphatase-inhibitor cocktail (Thermo Scientific™). After clearing of the sample (16.000 xg, 1
116 h at 4°C), the lysates were reduced (10 mM dithiothreitol), alkylated (50 mM chloroacetamide) and
117 digested (LysC; 1:75). Samples (800 µg) were diluted to 2 M urea and subjected to tryptic digestion
118 (1:50). After overnight incubation, phosphoenrichment was performed in the CECAD proteomics facility
119 using the Thermo Scientific™ Kit High Select TiO2 Kit (#A32993). All samples were analyzed as well by the
120 CECAD proteomics facility on a Q Exactive Plus Orbitrap mass spectrometer that was coupled to an EASY
121 nLC (both Thermo Scientific™). Peptides were loaded with solvent A (0.1% formic acid in water) onto an

122 in-house packed analytical column (50 cm, 75 µm inner diameter, filled with 2.7 µm Poroshell EC120 C18,
123 Agilent). Peptides were chromatographically separated at a constant flow rate of 250 nL/min using the
124 following gradient: 3-5% solvent B (0.1% formic acid in 80 % acetonitrile) within 1.0 min, 5-30% solvent B
125 within 121.0 min, 30-40% solvent B within 19.0 min, 40-95% solvent B within 1.0 min, followed by
126 washing and column equilibration. The mass spectrometer was operated in data-dependent acquisition
127 mode. The MS1 survey scan was acquired from 300-1750 m/z at a resolution of 70,000. The top 10 most
128 abundant peptides were isolated within a 1.8 Th window and subjected to HCD fragmentation at a
129 normalized collision energy of 27%. The AGC target was set to 5e5 charges, allowing a maximum
130 injection time of 55 ms. Product ions were detected in the Orbitrap at a resolution of 17,500. Precursors
131 were dynamically excluded for 25.0 s. All mass spectrometric raw data were processed with MaxQuant
132 (Tyanova, Temu and Cox, 2016) (version 2.2.0.0) using default parameters against the UniProt canonical
133 murine database (UP10090, downloaded 20.01.2023) with the match-between-runs option enabled
134 between replicates. Samples were sorted into two parameter groups, either containing the enriched or
135 non-enriched samples. Enriched samples had the phosphorylation (STY) variable modification added,
136 whereas non-enriched samples were quantified by LFQ. A follow-up analysis was done in Perseus 1.6.15
137 (Tyanova *et al.*, 2016). Results were cleaned up by removing hits from the decoy database, the
138 contaminant list and, in case of non-enriched fractions, those only identified by modified peptides were
139 removed. Afterwards, results were filtered for data completeness in at least one condition and LFQ
140 values (WP) or intensities (PP), imputed using sigma downshift with standard settings. Finally, FDR-
141 controlled two-sided t-tests between sample groups were performed (S0=0, FDR≤0.05) as well as a 1D
142 annotation enrichment using Perseus (version 1.6.15.0).

143 *Isolation and immortalization of mouse embryonic fibroblasts (MEFs)*

144 For the isolation of mouse embryonic fibroblasts (MEFs), timed matings were set up with one male and
145 two females of the desired genotype. At day 13, the pregnant mouse was anesthetized using isoflurane
146 (Piramal Healthcare) followed by a cervical dislocation. The lower abdomen was opened by an abdominal
147 incision to extract the two uterine horns. Embryos were isolated and transferred into a 24-well plate
148 filled with PBS. The head and the red organs (heart and liver) were removed. The rest of the embryo was
149 placed into a 12-well plate filled with 2 ml ice-cold 0.25 % Trypsin/PBS (diluted from 2.5 % Trypsin,
150 Gibco). The embryos were chopped into small pieces and incubated overnight at 4 °C. The trypsin
151 solution was discarded and the remaining Trypsin/tissue mixture was incubated for 30 min in a 37 °C
152 water bath. Afterward, medium (composition: DMEM/Glutamax, 10 % FCS, 1 % sodium pyruvate (100x),
153 1 % Pen Strep), was added, and the cell suspension was pipetted vigorously up and down to break up the

154 digested tissue into a single cell suspension. After 1 min, the cell suspension was collected, to remove
155 the sedimentation of the remaining tissue. This step was repeated and the cell suspension was filtered
156 through a 100 µm cell-strainer (Corning). Cells were plated and after 24 h, the medium was changed.
157 Immortalization of MEFs was performed as described previously (Todaro and Green, 1963). Briefly, cells
158 are split every three days and seeded with the same cell density. From passage three onwards, cells were
159 seeded on at least two 10 cm culture dishes. After around 15 passages, cells started to regrow. When
160 MEFs were immortalized, frozen back-ups were made.

161 *Isolation, immortalization, and BBS8 re-expression of urine renal epithelial cells (URECS)*

162 BBS8$^{c.915delG}$ patient urine (male; age 14) was collected at the University Hospital Essen, Germany, in
163 cooperation with the Network for early onset cystic kidney disease (Neocyst). . Urine sample was
164 centrifuged (10 min, 400 x g), and the pellet was resuspended in 10 ml washing buffer (sterile 1x PBS,
165 100 U Penicillin/Streptomycin (Gibco™), 500 ng/ml Amphotericin B (Sigma)). After centrifugation (10
166 min, 200 x g) the supernatant was removed leaving ~0.2 – 0.5 ml in the tube. The pellet was resuspended
167 in primary medium (PUC; DMEM-F12 (Sigma), REGM SingleQuot kit (Lonza, cat# CC-4127), 10% FBS
168 (Gibco™), 2 mM GlutaMAX (Gibco™), 1.0% Penicillin/ Streptomycin (Gibco™), 500 ng/ml Amphotericin B
169 (Sigma)) and plated in a single well of a galantine-coated 12-well plate. The plate was incubated for 48 h
170 at 37 °C, before the first PUC medium change. With the first visible colonies, PUC medium was changed
171 to normal growth medium (DMEM-F12 (Sigma), 10% FBS (Gibco™), 2 mM GlutaMAX (Gibco™), 1.0%
172 Penicillin/ Streptomycin (Gibco™)). Reaching a confluency of 60-80 %, cells were split in two wells of a 6-
173 well plate using TrypLE Select Express (Gibco™). One well was expanded, and stored as primary cells, and
174 one well was used for immortalization. Immortalization was started by adding 1 ml of previously
175 produced virus supplemented with 1 µl of Polybrene 8mg/ml (Sigma) to 40 % confluent cells and
176 incubated for 24 h at 37°C. The virus was removed and replaced by normal growth medium. Cells were
177 split thrice, while expansion in multiple 10 cm culture dishes before frozen back-ups were made.
178 Immortalized urine-derived renal epithelial cells (URECS) were additionally expressed exogenous with
179 viruses produced with pLenti6.3 F.hBBS8 and pLenti6.3 F.GFP in HEK293T cells. Sterilized harvest virus
180 supplemented with Polybrene was added to 40 % confluent cells and incubated for 24 h at 37°C. After
181 removing the virus, the cells were selected by adding normal growth medium supplemented with 0,001
182 mg/ml Blasticidin (Invivogen). Cells were split three times before selection was stopped and cells were
183 used for experiments.

184 *Cell culture and treatment*

185 Human embryonic kidney 293T cells (HEK293T, ATCC®), mIMCD3 cells, MEFs and URECs were cultivated
186 at 37°C and 5% CO_2. Thereby, HEK293T cells were maintained in DMEM + GlutaMAX™ medium (Gibco™)
187 supplemented with 10% fetal bovine serum (FBS, Gibco™), MEFs in DMEM/F-12 + GlutaMAX™ medium
188 (Gibco™) complemented with 10% FBS and 1% penicillin-streptomycin.URECs and mIMCD3 cells were
189 cultured in normal growth medium (DMEM-F12 (Sigma), 10% FBS (Gibco™), 2 mM GlutaMAX (Gibco™).
190 For URECs, 1.0% Penicillin/ Streptomycin (Gibco™) was added. All cell lines were tested negative for
191 mycoplasma (PCR Mycoplasma Test Kit I/C, PromoKine). To induce a higher amount of ciliogenesis,
192 mIMCD3 cells were grown in serum-free media for 24 h at 37°C. HEK293T cells were transiently
193 transfected with5 µg (IP) or 6 µg (Interactome) of F.hBBS8 in pcDNA6 using the calcium phosphate
194 method. As negative control, equal amounts of $F.EPS^{1-225}$ in pcDNA6 were used. The HDAC2 inhibitor
195 Tucidinostat (TUC, 160 nM; Biozol, cat# HY-109015) treatment was performed in serum-free media at
196 37°C for 24 h. Control treatment was performed with DMSO (AppliChem). For IF stainings, confluent
197 mIMCD3 cells were transfected with 5 µg of either F.EPS or F.HDAC2 using Lipofectamine®3000
198 (Invitrogen) in starvation medium and fixed 24 h after transfection. Every plasmid used for this study
199 added an N-terminal F9-tag to the protein of interest, which refers to a FLAG-tag followed by 9 histidine
200 residues. Only mHDAC2 was expressed with a single FLAG-tag.

201 *Harvest and fixation*

202 Cells were seeded in dishes or on glass coverslips in 12 well plates and incubated for 24 h, prior to
203 starvation or TUC treatment; both for an additional 24 h at 37°C. To harvest cells, they were washed with
204 PBS (1x), scraped in fresh PBS (1x), and centrifuged for 10 min, 10.000 rpm at 4°C. Cell pellets could be
205 used for western blot or RNA isolation. Harvest of whole cell lysate samples was performed by
206 resuspending the cells in cold 1x PBS followed by centrifugation for 5 min, 4.000 rpm at 4°C. Afterwards
207 cells were resuspended in 1x Laemmli with DTT and boiled for 5 min at 95°C. For Immunofluorescence
208 staining cells were fixed by adding 4% PFA (Walter CMP GmBH & Co) for 5 min, followed by methanol
209 (Roth) for 4 min. Fixed cells were washed thrice with PBS (1x) before staining.

210 *Cilia stability assay*

211 Depolymerization of microtubules was induced by incubating starved cells for 30 min on ice. The
212 subsequent fixation was continuously performed on ice. The untreated control cells were fixed at room
213 temperature. Fixed cells were stored at 4°C in PBS until staining and quantifying cilia.

214 *Quantitative real-time PCR*

215 RNA isolation was performed from kidney tissue samples, thereby using one-quarter of a kidney. Tissue
216 was ground with BeadBeater (Roth) using a Precelly24 with 5.000 rpm two times for 30 s in Tri-Reagent.
217 RNA isolation from cells was performed by resuspending snap-frozen cell pellets in Phenol. RNA
218 extraction was performed with the Direct-zol RNA Miniprep kit (Zymo Research) following the
219 manufacturer's instructions, including a DNase1 treatment step. Before the reverse transcription using
220 the High-Capacity cDNA Reverse Transcription kit (Applied Biosystems), RNA concentration and sample
221 quality were assessed on a Nanodrop spectrophotometer (Peqlab). mRNA was assessed by qPCR with
222 SYBR Green (Thermo Scientific™) using mHprt1 or hHPRT1 as endogenous control. The qPCR experiments
223 were performed on a QuantStudio Q5 Real-time PCR System (ThermoFisher Scientific). For data analysis,
224 all results were normalized to the housekeeping gene *Hprt1* using the delta-delta CT followed by a two-
225 tailed Student's *t*-test ($p<0.05$).

226 *Co-Immunoprecipitation*

227 Co-immunoprecipitation (Co-IP) was performed as previously described (Habbig *et al.*, 2011) using the IP
228 Buffer (20 mM Tris, 1% (v/v) TritonX-100, 50 mM NaCl, 15 mM $Na_4P_2O_7$, 50 mM NaF, pH 7.5)
229 supplemented with inhibitors (44 µg/µl PMSF, 2 mM Na_3VO_4) in four replicates. Input samples (lysates)
230 were collected, and the remaining samples were incubated with α-FLAG M2 Beads (A2220, Sigma-
231 Aldrich) for 2 h. Samples were denatured and reduced in 2x Laemmli before SDS-PAGE. For proteomic
232 analysis, the IP Buffer was supplemented with cOmplete™ Protease Inhibitor Cocktail (Roche). After
233 sonication, the lysates were first centrifuged 30 min at 14.000 g at 4°C followed by ultracentrifugation
234 for 45 min at 100.000 g and 4°C. After three washing steps the beads were incubated with 5% SDS in PBS
235 for 5 min at 95 °C, followed by reduction with 10 mM dithiothreitol and alkylation with 40 mM
236 chloroacetamide.

237 *Interactome*

238 Samples were analyzed by the CECAD Proteomics Facility on an Orbitrap Exploris 480 (Thermo Scientific,
239 granted by the German Research Foundation under INST 1856/71-1 FUGG) mass spectrometer equipped
240 with a FAIMSpro differential ion mobility device that was coupled to an Vanquish neo in trap-and-elute
241 setup (Thermo Scientific). Samples were loaded onto a precolumn (Acclaim 5µm PepMap 300 µ
242 Cartridge) with a flow of 60 µl/min before reverse-flushed onto an in-house packed analytical column (30
243 cm length, 75 µm inner diameter, filled with 2.7 µm Poroshell EC120 C18, Agilent). Peptides were
244 chromatographically separated with an initial flow rate of 400 nL/min and the following gradient: initial
245 2% B (0.1% formic acid in 80 % acetonitrile), up to 6 % in 3 min. Then, flow was reduced to 300 nl/min

246 and B increased to 20% B in 26 min, up to 35% B within 15 min and up to 98% solvent B within 1.0 min
247 while again increasing the flow to 400 nl/min, followed by column wash with 98% solvent B and re-
248 equilibration to initial condition. The FAIMS pro was operated at -50V compensation voltage and
249 electrode temperatures of 99.5 °C for the inner and 85 °C for the outer electrode. The mass
250 spectrometer was operated in data-dependent acquisition top 24 mode with MS1 scans acquired from
251 350 m/z to 1400 m/z at 60k resolution and an AGC target of 300%. MS2 scans were acquired at 15 k
252 resolution with a maximum injection time of 22 ms and an AGC target of 300% in a 1.4 Th window and a
253 fixed first mass of 110 m/z. All MS1 scans were stored as profile, all MS2 scans as centroid. All mass
254 spectrometric raw data were processed with Maxquant (version 2.4) (Tyanova, Temu and Cox, 2016)
255 using default parameters against the Uniprot HUMAN canonical database (UP5640) with the match-
256 between-runs option enabled between replicates. Follow-up analysis was done in Perseus 1.6.15
257 (Tyanova *et al.*, 2016). Protein groups were filtered for potential contaminants and insecure
258 identifications. Remaining IDs were filtered for data completeness in at least one group and missing
259 values imputed by sigma downshift (0.3 σ width, 1.8 σ downshift). Afterwards, FDR-controlled two-sided
260 t-tests were performed (S0=0, FDR≤0.05). Protein structure prediction was done using the Alphafold
261 server (Abramson *et al.*, 2024), while ChimeraX has been used for visualization (Pettersen *et al.*, 2021;
262 Meng *et al.*, 2023).

263 *Immunoblotting*

264 Confluent grown , and starved MEF cells were harvest with RIPA buffer (50 mM Tris/HCl, 150 mM NaCl,
265 1% (v/v) NP-4O, 0.5% (w/v) Sodium deoxycholate, 0.1% (w/v) SDS), supplemented with 1% Halt Protease
266 and Phosphatase Inhibitor Cocktail (Thermo Scientific™) (Brücker *et al.*, 2023). Cells were lysed on ice
267 and sonicated for 2 s. Protein concentration of lysates was determined and loaded onto a 10% SDS-PAGE
268 and subsequently transferred to a PVDF-FL membrane (Millipore). URECSs cell pellets were lysed in
269 adjusted inhibitor-supplemented RIPA buffer (50 mM Tris/HCL pH 7.5, 150 mM NaCl, 0.1 % NP-40, 0.5 %
270 Na-Deoxycholat, 0.1 % SDS) supplemented with Benzonase® (70746-3 Millipore), cOmplete™
271 (4693159001, Roche) and PhosSTOP™ (4906845001, Roche), on ice for 30 min. This is followed by
272 centrifugation for 1 h, 14.000 rpm at 4°C, determination of protein concentration, and supplementing
273 and boiling with 5x Laemmli. Samples were loaded onto a gel as before and transferred to a PVDF
274 membrane (Millipore), including whole cell lysates of mIMCD3 cells in 1x Laemmli. After blocking,
275 membranes were incubated overnight at 4°C in primary antibodies (FLAG, F7425, Sigma-Aldrich, 1:1000;
276 HDAC2, ab32117 Abcam, 1:1000; acetylated Tubulin, T6793 Sigma, 1:1000; Calnexin, 10427-2 AP
277 ProteinTech, 1:1000). Secondary antibodies were incubated for 1 h at RT either fluorescent (Li-COR

278 Biosciences IRDye680 and IRDye800 1:10.000: rb680, 925-68073; mm680, 925-68072; rb800, 925-32213)
279 or horseradish peroxidase-conjugated antibodies. Fluorescent signals were visualized using the Odyssey
280 Infrared Imaging System 2800 (Li-COR), for peroxidase-conjugated ECL detection, and images were
281 acquired with a Fusion Solo S (Vilber Lourmat Germany GmbH, Eberhardzell, Germany).

282

283 *Immunofluorescence, Immunochemistry and TUNEL staining*

284 The kidney tissue staining of 4 µm (cilia staining) and 2 µm (other stainings) fixed sections were
285 performed as previously described (Dafinger *et al.*, 2021). The primary antibodies (NF-kB, #8242 Cell
286 Signaling, 1:1000; CD3, MCA-1477 Biorad, 1:100; acetylated Tubulin, T6793 Sigma, 1:1000; Slc12a3,
287 HPA028748, Sigma Aldrich, 1:500; ARL13B, 17711-1-AP ProteinTech, 1:500) were incubated overnight at
288 4°C, followed by incubation with secondary antibodies. For immunochemistry, the DBA kit (K3468 DAKO,
289 30 min for NF-kB; SK-4105 Vector, 5 min for CD3) was used and samples counterstained with
290 Hematoxylin. For immunofluorescence, fluorophore-coupled antibodies (Jackson ImmunoResearch,
291 1:500: anti-mouse-Cy5, # 715-175-150; anti-rabbit A647, 711-605-152; anti-mouse-Cy3, 715-165-150;
292 and FITC-Lotus Tetragonolobus Lectin (LTL), FL-1321-2; Vector laboratories, 1:500) were used for 1 h at
293 RT. Samples were mounted after a short incubation with Hoechst 33342 (ThermoFisher Scientific,
294 1:5000) with ProLong™ Diamond (ThermoFisher Scientific). The DeadEnd™ Fluorometric TUNEL System
295 (Promega) was performed following the manufacturer's instructions, with the exception that the
296 samples were mounted, with a pre-incubation of Hoechst with ProLong™ Diamond. Fixed MEFs were
297 quenched with 50 mM NH_4Cl for 10 min, before permeabilisation with 0,3% PBS-TritonX-100 for 20 min.
298 Antibodies were diluted in Fish-Block (0.1 % (w/v) ovalbumin, 0.5 % (w/v) fish gelatine, in PBS),
299 supplemented with 0,3% TritonX-100. The primary antibody (ARL13B 1:800 cat# ab136648, Abcam;
300 acetylated Tubulin, 1:800 cat# T6793, Sigma) were incubated overnight at 4°C followed by the secondary
301 antibodies (anti-rabbit 488, A11034 Invitrogen, 1:400; anti-mouse 555, A31570, Invitrogen, 1:400; DAPI,
302 Roth, 1:400). Finally, coverslips were mounted with Fluoromount-G (ThermoFisher, 00-4958-02) and
303 imaged with the Leica microscope CTR6000, with DM6000B Laser and DFC360FX camera. MEF cell
304 images were deconvoluted with the Leica imaging software LASX. Cilia number and length were
305 determined with the open-source Fiji software (Schindelin *et al.*, 2012). Fixed BBS8$^{c.915delG}$ URECs were
306 blocked for 1 h in PBS containing 0.1 % triton-X-100 and 5 % normal donkey serum. Fixed mIMCD3 cells
307 were permeabilized for 10 min with 0.1 % triton X-100 diluted in PBS followed by a 1 h blocking step with
308 10 % NDS in PBS supplement with Ca^{2+} and Mg^{2+}. The primary antibody (ARL13B 1:1000 cat# ab136648,
309 Abcam; ARL13b 1:400, cat# 17711-1-AP, Proteintech; phospho-HDAC6 1:500 cat# PA5-105035,

310 Invitrogen; acetylated Tubulin 1:1000, Sigma; beta-Tubulin 1:50, cat# E7, DSHB) were incubated at 4°C.
311 Secondary Antibodies (donkey anti-mouse Cy3, cat# 715-165-150, Jackson ImmunoResearch; donkey
312 anti-rabbit A647, cat# 711-605-152, Jackson ImmunoResearch; DYKDDDDK Tag (L5), Alexa Fluor™ 488,
313 1:500; Invitrogen) were incubated at RT. Nuclei staining was performed with Hoechst 33342 Solution
314 (1:5000, cat# H3570 Invitrogen). Finally, coverslips were mounted with ProLong™ Diamond w/o DAPI
315 (cat# P36965, Thermo Fisher Scientific). URECs and IMCD3 cells were imaged with the AxioObserver
316 microscope with an axioCam ICc1, Axiocam 702 mono, Apoptome system (Carl Zeiss MicroImaging, Jena,
317 Germany). Images were exported through Zen Blue Software by Zeiss and aligned together using the free
318 design tool Inkscape.

319 *Quantification and statistical analysis*

320 Data are expressed as mean ± standard deviation (SD). All experiments were performed in at least 3
321 independent biological replicates. The data were statistically analyzed with GraphPad Prism version 9.5.1
322 unless otherwise mentioned. Statistical testing was performed as indicated in the figure legends.

323 **Results and discussion**

324 *Cystic kidney disease in Bbs8 knockout mice is accompanied by inflammation and fibrosis*

325 To investigate the function of BBS8 in the kidney, we analyzed the kidneys of a conventional *Bbs8*$^{-/-}$
326 mouse line (Tadenev *et al*., 2011) where a mild renal phenotype with moderately dilated tubules in the
327 deep cortical region has previously been reported at 8 months of age. Consistent with this, no apparent
328 renal abnormalities were observed at 24 weeks. Therefore, we extended the observation period to 46
329 weeks. At this age, *Bbs8*$^{-/-}$ mice exhibited marked obesity, with a body weight approximately 30% higher
330 than that of control animals **(Fig. 1A)**, consistent with a typical BBS phenotype. In addition, signs of renal
331 involvement began to emerge, as indicated by a trend toward elevated serum urea levels **(Fig. 1B)** and a
332 slight increase in kidney weight **(Supp. Fig. 1A)**, although these changes did not reach statistical
333 significance. PAS staining of kidney sections revealed cyst formation and tubular dilatation **(Fig. 1C)**, with
334 a cyst index approximately six-fold higher in Bbs8$^{-/-}$ compared to control mice **(Fig. 1D)**. Further analysis
335 revealed that although the size of individual cysts detected in *Bbs8*$^{-/-}$ was similar to the size of dilated
336 tubules and cysts occasionally found in age-matched control animals **(Supp. Fig. 1B)**, the number of
337 dilated tubules and cysts was significantly increased **(Supp. Fig. 1C)**. Staining for proximal and distal
338 tubules in the kidney revealed that the majority of cysts originated from distal tubules, as they were
339 positive for Slc12a3 **(Fig. 1E)**. Furthermore, *Bbs8*$^{-/-}$ kidneys showed a significant increase in inflammation
340 and fibrosis in PAS and Masson's trichrome stained sections **(Fig. 1F)**. In line with inflammation and

341 fibrosis, we observed an accumulation of T-cells ($CD3^+$), as well as an increased nuclear expression of the
342 NF-κB subunit RelA/p65, in particular in inflammation-rich areas (arrowheads) but also in kidney tubules
343 (arrows), in *Bbs8*$^{-/-}$ kidney tissue **(Fig. 1G)**. Increased TUNEL-positive cells indicated ongoing cell death in
344 *Bbs8*$^{-/-}$ kidneys **(Fig. 1H)**. To unravel the role of potential players involved in these processes of cell death,
345 we found the mRNA transcription of *RelA/p65*, as well as, of the pyroptosis markers *Nlrp3* and *GsdmD* to
346 be significantly increased **(Fig. 1I)**. Taken together, *Bbs8*$^{-/-}$ mice, in addition to obesity, fatty liver disease,
347 retinal degeneration, and occasional polydactyly, develop a relatively late-onset cystic fibrotic kidney
348 disease accurately reflecting the patient renal manifestation. Cyst formation predominantly originates
349 from the distal tubular segments and increased renal expression of genes associated with pyroptosis and
350 the inflammasome, key factors of renal fibrosis and inflammation.

351 *The loss of Bbs8 affects ciliary tubulin acetylation and primary cilia stability*

352 Since BBS8 is a component of the BBSome and the role of cilia in Bardet-Biedl syndrome (BBS) is well
353 established, we next examined primary cilia in kidney tissue from *Bbs8*$^{-/-}$ mice. In contrast to mouse
354 olfactory tissue, where a dramatic loss of cilia had been described (Tadenev *et al.*, 2011), we did not
355 observe any significant difference in the number and length of cilia in kidney sections of *Bbs8*$^{-/-}$ mice
356 compared to wildtype littermates **(Fig. 2A)**. Since quantification of cilia in tissue sections has technical
357 limitations, we also used mouse embryonic fibroblasts (MEFs) generated from *Bbs8*$^{-/-}$ and control mice. A
358 high percent of MEFs typically form cilia, and quantification of cilia number and length via ARL13B
359 staining revealed no significant difference in serum-starved MEFs **(Fig. 2B)**, confirming our finding in the
360 kidney sections. As an additional model, we isolated URECs from a BBS8 patient with a homozygous BBS8
361 variant (BBS8$^{c.915delG}$) that results in a frameshift and premature protein termination (p.Met305Ilefs*15).
362 In these cells we re-expressed F.hBBS8 or F.GFP via lentiviral gene transfer. Expression was validated by
363 immunoblotting (**Suppl Fig. 2A**). Consistently, cilia numbers as determined by ARL13B staining were not
364 significantly different in these cell lines **(Fig. 2C)**. Surprisingly, however, we observed a discrepancy
365 between ARL13B staining and acetylated tubulin, another classical ciliary marker: in kidney sections **(Fig.
366 2E)**, as well as in MEFs **(Fig. 2F)** and URECs **(Fig. 2G)**, a significant number of cilia in the BBS8-deficient
367 group identified by ARL13B staining were negative for acetylated tubulin staining. Taking into account
368 that tubulin K40 acetylation is important for microtubule and, thus, ciliary stability, we analyzed this in
369 the BBS8$^{c.915delG}$ URECs with and without re-expression of F.hBBS8 by incubating the cells on ice to
370 depolymerize microtubules and destabilize cilia. This assay revealed that upon treatment, the amount of
371 cilia was significantly reduced in BBS8$^{c.915delG}$ F.GFP URECs as compared to the rescued cells **(Fig. 2H/I)**.

372 Thus, the loss of BBS8 does not affect cilia number but leads to a reduction of acetylated tubulin within
373 the cilium, which in turn impacts ciliary stability.

374 *Proteomic analysis of Bbs8-deficient kidneys*

375 To gain more insights into the kidney pathology and to decipher the mechanism contributing to the loss
376 of tubulin acetylation, we performed unbiased proteomic expression analysis of kidney lysates from
377 *Bbs8*$^{-/-}$ and control mice**.** The principal component analysis clearly separated the two genotypes in both
378 datasets **(Fig. 3A)**. After quality control (QC), we found a total of 2926 proteins in the whole proteome
379 (WP) **(Fig. 3B; Suppl. Table 1)**. Based on the Student's *t*-test (S0=0; FDR≤0.05), only 10 proteins were
380 significantly up- and 16 significantly downregulated in *Bbs8*$^{-/-}$ kidney lysates compared to control **(Fig.**
381 **3C).** Among those differentially expressed proteins were several proteins previously associated with
382 ciliopathies, cystogenesis, and kidney disease progression: For example, dynein cytoplasmic 2 heavy
383 chain 1 (DYNC2H1) and dystrobrevin binding protein 1 (DTNBP1) were found to be downregulated in the
384 knockout. DYNC2H1, a subunit of the IFT-dynein motor, drives retrograde IFT-rafts and plays a role in the
385 formation of the ciliary transition zone. Mutations lead to a skeletal ciliopathies, namely Jeune
386 asphyxiating thoracic dystrophy, short-rib polydactyly, and also to non-syndromic retinal degeneration
387 (Jensen *et al.*, 2018; Vig *et al.*, 2020; Hammarsjö *et al.*, 2021; Piceci-Sparascio *et al.*, 2023). Mutations in
388 *DTNBP1,* encoding a subunit of the biogenesis of lysosome-related organelles complex-1 (BLOC-1), cause
389 late-onset cystic kidney disease in mice (Monis, Faundez and Pazour, 2017). Proteins with increased
390 expression compared to control included retinol-binding protein 4 (RBP4), uromodulin (UMOD),
391 nucleoporin 98 (NUP98), and histone deacetylase 2 (HDAC2), each of which has previously been
392 associated with kidney diseases or primary cilia (Zaucke *et al.*, 2010; Kobayashi *et al.*, 2017; Endicott and
393 Brueckner, 2018; Xun *et al.*, 2018). Given our finding of decreased acetylated ciliary tubulin, we were
394 surprised to find neither the key acetylation enzyme αTAT1 nor the deacetylase HDAC6 to be
395 significantly altered. Previous studies have shown that HDAC6 upon phosphorylation by Aurora A kinase
396 (AurA) promotes tubulin deacetylation in cilia and ciliary disassembly (Pugacheva *et al.*, 2007). This
397 process can be prevented by BBS proteins through the recruitment of Inversin/NPHP2 to the ciliary base
398 (Patnaik *et al.*, 2019). However, AurA levels were not significantly changed, and phosphoproteomic (PP)
399 analyses performed in parallel **(Suppl. Fig. 3A/B; Suppl. Table 1**) also showed no alteration in HDAC6 or
400 AurA phosphorylation. Similarly, localization and expression levels of pHDAC6 in urine-derived
401 BBS8$^{c.915delG}$ URECs at the ciliary base was not altered **(Suppl. Fig. 3C)**. However, our data revealed a
402 significantly increased expression of another histone-deacetylase, HDAC2, in *Bbs8*$^{-/-}$ kidneys. This finding

403 could be further confirmed by Western blot experiments in both MEFs **(Fig. 3D)** and BBS8-deficient
404 URECs **(Fig. 3E)**.

405 *BBS8 co-precipitates with HDAC2*

406 Intrigued by upregulation of HDAC2 upon loss of BBS8, we questioned whether there might be a
407 connection between BBS8 and HDAC2 in the context of a shared protein complex. For an unbiased
408 interactomic analysis, we exogenously expressed F.hBBS8 or an equally FLAG-tagged control protein in
409 HEK293T cells and performed an anti-FLAG immunoprecipitation followed by MS/MS. The principal
410 component analysis clearly separated the F.hBBS8 pulldown from the control **(Fig. 4A)**. We identified
411 1151 proteins of which 986 were significantly enriched upon precipitation with BBS8 **(Fig. 4B, Suppl.**
412 **Table 2)**. Notably, among those were many known members of the BBSome (BBS1, BBS2, BBS4, BBS5,
413 BBS7, BBS9) and the BBS chaperonin complex (CCT6A, CCT5, CCT3, CCT2, TCP1, CTT8, CCT4 and CCT7).
414 We again found HDAC2 as the only enriched histone-deacetylase. Additional protein groups shown to
415 potentially interact with BBS8 include heat shock binding proteins and proteins related to the Wnt
416 signaling pathway **(Supp. Fig. 4A)**. To confirm this potential interaction, we performed a similar co-
417 immunoprecipitation experiment and were able to detect endogenous HDAC2 upon pull down with
418 BBS8. **(Fig. 4C)**. Co-immunoprecipitation in the reverse direction confirmed BBS8 co-precipitating with
419 F9.HDAC2 **(Fig. 4D)**.

420 *HDAC2 induces the deacetylation of alpha tubulin*

421 HDAC2 has previously been associated with reduced cilia number in pancreatic ductal adenocarcinoma, a
422 phenomenon attributed to increased transcription of AurA and consequently enhanced ciliary
423 disassembly by HDAC6 (Kobayashi *et al.*, 2017). However, our data from *Bbs8*$^{-/-}$ tissue provided no
424 evidence for elevated AurA expression or HDAC6 activity. Therefore, we aimed to demonstrate that
425 HDAC2 directly influences tubulin acetylation. To this end, we transiently transfected HEK293 cells with
426 F.mHDAC2 or F.GFP and included F.hHDAC6 as a positive control. Immunoblot analysis of cell lysates
427 revealed that HDAC2 expression reduced of overall cellular levels of K40-acetylated α-tubulin, albeit to a
428 slightly lesser extent than HDAC6 **(Fig. 5A).** This functional similarity between HDAC2 and HDAC6 is
429 further supported by structural predictions using AlphaFold. The acetylated K40 residue of tubulin is
430 predicted to interact with the HDAC domain of HDAC2 in a manner similar to its interaction with the
431 second HDAC domain of HDAC6 **(Suppl. Fig. 5)**. To further substantiate that the loss of ciliary tubulin
432 acetylation in BBS8-deficient cells is attributable to HDAC2 activity, we employed the selective HDAC
433 inhibitor Tucidinostat (TUC). TUC is a specific low nanomolar inhibitor of the class I HDAC enzymes

434 (HDAC1/2/3; EC50: 100-200 nM) and class IIb HDAC enzymes (HDAC10; EC50: 100 nM) with almost no
435 effect on HDAC6 (EC50 >10 µM) and has already been used in a clinical trial for patients relapsed or
436 refractory peripheral T-cell lymphomas (Ho, Chan and Ganesan, 2020; Liu *et al.*, 2021; Utsunomiya *et al.*,
437 2022). We treated the urine-derived BBS8$^{c.915delG}$ URECs expressing F.GFP or F.BBS8 with TUC (160 nM) or
438 DMSO for 24 h in serum-free medium and stained for primary cilia with antibodies directed against
439 ARL13B and acetylated-tubulin. As before, we observed in the control group (DMSO) a significantly
440 decreased percentage of acetylated-tubulin positive cilia in the urine-derived BBS8$^{c.915delG}$ URECS as
441 compared to BBS8 re-expression. However, HDAC2-inhibition significantly increased the percentage of
442 acetylated-tubulin positive cilia in BBS8$^{c.915delG}$ cells, to a similar level as BBS8 re-expression did **(Fig. 5B)**.

443 In summary, we conclude that loss of BBS8 results in a pathological upregulation of HDAC2 activity,
444 which targets acetylated α-tubulin within the cilium, thereby perturbing ciliary dynamics and stability.
445 Consistent with the relatively mild and late-onset kidney phenotype, these changes do not result in
446 major alterations of cilia and have no impact on cilia length or number. Nevertheless, these subtle
447 modifications in primary cilia architecture may affect ciliary dynamics and, over time, negatively
448 influence the homeostasis of renal tissue. Thus, HDAC2 may indeed represent a promising therapeutic
449 target. Supporting this notion, a chemical screen in two zebrafish models of polycystic kidney disease
450 (PKD) identified both a pan-HDAC inhibitor and a class I HDAC inhibitor as suppressors of cyst formation
451 (Cao *et al.*, 2009). Our study provides a mechanistic basis for this positive effect of HDAC inhibitors by
452 identifying the HDAC2-induced acetylation-defect of cilia which can be reversed by a class 1 inhibitor as
453 potential driver of cystogenesis in BBS8, linked to subtle ciliary defects.

454 **Data Availability**

455 The mass spectrometry proteomics data have been deposited to the ProteomeXchange Consortium via
456 the PRIDE (Perez-Riverol *et al.*, 2024) partner repository with the dataset identifier PXD064988
457 (interactome) and PXD064990 (proteomeBBS8-/- kidneys). Login details are available from the authors
458 upon request.

459 **Figure legends:**

460 *Figure 1. Bbs8$^{-/-}$ mice develop late-onset cystic kidney disease with fibrosis and inflammation.*

461 46-week-old *Bbs8$^{-/-}$* compared to control (*Bbs8$^{+/+}$*) mice showed a significantly increased **(A)** body weight
462 (n=4) and an increasing trend **(B)** of measured urea level of blood serum (n=4). **(C)** PAS staining of the
463 whole kidney in control and *Bbs8$^{-/-}$* animals, showing cyst formation in the knockout; Scale bar: 1 mm. **(D)**

464 Cyst index described in a cyst-to-tissue area ratio, normalized to control animals (n=4). **(E)** Staining of
465 distal (Slc12a3, magenta) and proximal tubules (LTL, green) in the kidney showing cyst formation in the
466 distal convoluted tubules; Scale bar: 500 µm. **(F)** Representative microscopic images of the PAS staining
467 (higher magnified area), showing clusters of inflammation (Arrow; Scale bar: 200 µm). The additional
468 Masson's trichrome staining, displayed fibrosis in *Bbs8*$^{-/-}$ animals (Arrowhead; Scale bar: 300 µm). **(G)**
469 Representative microscopic images of CD3^{+} and NF-kB (RelA/p65) expression revealed inflammation in
470 *Bbs8*$^{-/-}$ animals; Scale bar: 300 µm. **(H)** TUNEL staining of control and Bbs8$^{-/-}$ kidney tissue; Scale bar: 100
471 µm. **(I)** Quantitative real-time PCR of *RelA/p65* and inflammasome genes in control and *Bbs8*$^{-/-}$ kidney
472 samples (n=4). All of the statistical analyses were performed using a two-sided Student's *t*-test (*p*-value:
473 <0.001***; 0.002**; 0.033*; ns=0.12).

474 *Figure 2. BBS8 deficiency results in reduced ciliary tubulin acetylation and stability without significantly*
475 *affecting the number or length of cilia.*

476 **(A)** Control and *Bbs8*$^{-/-}$ kidney tissue stained for cilia using ARL13B antiserum (Scale bar: 50 µm). **(B)** *Bbs8*$^{-}$
477 $^{/-}$ and control mouse embryonic fibroblasts (MEF) quantified for the number and length of cilia by
478 ARL13B staining (n=4), statistically analyzed using an unpaired Student's *t*-test (*p*-value: <0.001***;
479 0.002**; 0.033*; ns=0.12). **(C)** BBS8$^{c.915delG}$ and BBS8 re-expressing URECs stained for cilia using ARL13B
480 antiserum (n=7), statistically analyzed using an unpaired Student's *t*-test (*p*-value: <0.001***; 0.002**;
481 0.033*; ns=0.12). **(D-F)** Representative images of primary cilia co-stained for ARL13B (green) and
482 acetylated-tubulin (ac-Tub, magenta; scale bar: 10 µm); graphs showing the percentage of cells with a ac-
483 Tub positive cilium from the total amount of cilia, as identified by ARL13B staining. Arrowhead indicates
484 ac-Tub negative cilia. Statistically analyzed using an unpaired Student's *t*-test (*p*-value: <0.001***;
485 0.002**; 0.033*; ns=0.12). Staining and analysis were performed in **(D)** control and *Bbs8*$^{-/-}$ kidney
486 tissue (n=3), **(E)** cultured *Bbs8*$^{-/-}$ and control MEFs (n=4), **(F)** BBS8$^{c.915delG}$ patient-isolated URECs stably
487 expressing either F.hBBS8 or F9.GFP (n=4). **(G)** Cilia stabilization assay was performed in BBS8$^{c.915delG}$
488 patient-isolated URECs stably expressing either F.hBBS8 or F.GFP. Destabilization was induced by keeping
489 the cells for 30 min on ice. Representative images of primary cilia stained for ARL13B (green; n=3; Scale
490 bar: 10 µm). Statistical analysis was performed by using a one-way ANOVA followed by a two-sided
491 Student's *t*-test (*p*-value: >0.001***; 0.002**; 0.033*; ns=0.12).

492 *Figure 3. HDAC2 is one of the few proteins significantly upregulated in BBS8*$^{-/-}$ *kidney tissue*

493 **(A)** Principal component analysis (PCA) plot of the whole proteome (WP) of control and *Bbs8*$^{-/-}$ kidney
494 samples. The axes represent the percentages of variation explained by the principal components, three

495 biological replicates per group. **(B/C)** Scatter blot of the proteome. Significantly (FDR≤0.05) up-regulated
496 (yellow, 1-10) or downregulated (cyan, 1-16) proteins are marked and additionally listed in the table. **(D)**
497 Lysates from control and *Bbs8*$^{-/-}$ mouse embryonic fibroblasts (MEFs) were immunoblotted against
498 HDAC2, with Calnexin as loading control. **(E)** Urine-derived BBS8$^{c.915delG}$ URECs stably expressing either
499 F.hBBS8 or F.GFP were immunoblotted against HDAC2 with Calnexin as a loading control.

500

501

502 *Figure 4. BBS8 and HDAC2 are components of a common protein complex*

503 **(A)** Principal component analysis (PCA) plot of the interactome data of F.hEPS and F.hBBS8 in HEK293T
504 cells. The axes represent the percentages of variation explained by the principal components. Four
505 individual replicates were performed. **(B)** Scatter plot of the interactome, marked with potential
506 interactors of BBS8 (FDR≤0.05) in magenta. **(C)** Co-IP from HEK293T cells, expressing F.hBBS8 or F.hEPS
507 as control. Immuno-precipitation from lysates was done with α-FLAG (IP), immunoblot was performed
508 with α-HDAC2 and with α-FLAG. **(D)** Co-IP from HEK293T cells expressing F.mHDAC2 or F.hEPS together
509 with eGFP.hBBS8. Immuno-precipitation from lysates was performed with α-FLAG (IP), immunoblot with
510 α-eGFP and α-FLAG.

511 *Figure 5. HDAC2 promotes tubulin deacetylation, and its inhibition increases tubulin acetylation in BBS8-*
512 *deficient cells.*

513 **(A)** Lysates of HEK293T cells transfected with F.hEPS, F.mHDAC2, F.hHDAC6 and co-transfected with
514 F.GFP were immunoblotted with α-acetylated tubulin and α-FLAG. F.GFP expression was used as control
515 for quantitative comparison (n=3) with the statistical analysis of a one-way ANOVA followed by a two-
516 sided Student's *t*-test (*p*-value: >0.001***; 0.002**; 0.033*; ns=0.12). Data were normalized to the
517 acetylated tubulin amount in F.hEPS expressing cells. **(B)** BBS8$^{c.915delG}$ patient-isolated URECs stably
518 (re)expressing either F.hBBS8 or F.GFP were treated with the HDAC2 inhibitor Tucidinostat (TUC, 160
519 nM) or DMSO as control. Representative images of primary cilia co-stained with the cilia marker ARL13B
520 (green) and acetylated-tubulin (ac-Tub, magenta; scale bar: 10 µm) displaying the restoration of
521 acetylation within primary cilia in F.GFP BBS8$^{c.915delG}$ URECs upon HDAC2 inhibition (n=4; arrowheads: ac-
522 Tub positive cilia; arrows: ac-Tub negative cilia); graph showing the percentage of acetylated-tubulin
523 positive cilia of the total amount of cilia determined by ARL13B staining. Statistical analysis was

524 performed by using a one-way ANOVA followed by a two-sided Student's *t*-test (*p*-value: >0.001***;
525 0.002**; 0.033*; ns = 0.12).

526 *Supplementary Figure 1. Small-cyst formation in Bbs8$^{-/-}$ kidney and systemic inflammation.*

527 **(A)** Kidney weight of 46-week-old control and *Bbs8*$^{-/-}$ mice did not significantly alter (n=4). **(B)** The
528 measured cyst area is depicted as jittered dots with the mean as a horizontal line. The values are plotted
529 on a $\log_{10}$ scale. Single individuals are plotted separately (n=4). **(C)** The overall number of cysts is
530 significantly increased in *Bbs8*$^{-/-}$ animals (n=4). For statistical analysis, a two-sided Student's *t*-test *was*
531 *used* (*p*-value: <0.001***; 0.002**; 0.033*; ns = 0.12).

532

533 *Supplementary Figure 2. Re-expression of BBS8 in* BBS8$^{c.915delG}$ URECs

534 **(A)** Urine-derived BBS8$^{c.915delG}$ URECS stably expressing either F.hBBS8 or F.GFP, were immunoblotted
535 against FLAG with Calnexin as control.

536 *Supplementary Figure 3. Additional analyses of the phosphoproteome data*

537 **(A)** Principal component analysis (PCA) plot of the phosphoproteome (PP) data of control and *Bbs8*$^{-/-}$
538 kidney samples. The axes represent the percentages of variation explained by the principal components.
539 Three individual replicates were performed. **(B)** Analysis of the PP identified 6223 phosphosites, within a
540 total of 2188 individual proteins from which 151 were significantly up- and 1041 were significantly down-
541 regulated. Among these were multiple HDAC2 phospho-peptides containing 3 serine (Ser) residues:
542 Ser394, Ser422 and Ser424. Notably, HDAC6 was not found to be changed in its phosphorylation. **(C)** Co-
543 Staining for the cilia (ARL13B, green) and phopho-HDAC6 (orange) in urine-derived BBS8$^{c.915delG}$ URECs re-
544 expressing F.hBBS8 or F.GFP (Scale bar: 10 µm). Ciliary base is indicated by arrowheads.

545 *Supplementary Figure 4. BBS8 interactors involved in cilia signaling pathways*

546 **(A)** Scatter plot of different protein clusters expressed in the BBS8 interactome for different GO-terms:
547 BBSome, chaperonin-containing T-complex, heat shock protein binding and Wnt signaling pathway.

548 *Supplementary Figure 5. Modeling the interaction of HDAC2 and HDAC6 with K40-acetylated alpha*
549 *Tubulin.*

550 **(A)** Human TBA1A (UniProt ID: Q71U36) with the PTM "N6-acetyl-L-lysine" added to K40 was co-
551 predicted in AlphaFold with the HDAC domain of HDAC2 (Q92769; residues 9–322) or the second HDAC

552 domain of HDAC6 (Q9UBN7; residues 482–800), a well-characterized tubulin deacetylase. The ipTM and
553 pTM values were obtained from the AlphaFold server. The acetylated residue K40 is highlighted in red.

554 *Supplementary Figure 6. Original data: full-sized immunoblots.*

555 Original western blots only cropped to gel size **(A)** of Supp. Figure 2 A, **(B)** of Figure 3 D, **(C)** of Figure 3 E,
556 **(D)** of Figure 4 C, **(E)** of Figure 4 D and **(F)** of Figure 5 A. To visualize the expression of F.hBBS8, the
557 membrane was captured with a short and longer exposure time.

558

559

560 **References:**

561 Abramson, J. *et al.* (2024) 'Accurate structure prediction of biomolecular interactions with AlphaFold 3',
562 *Nature 2024 630:8016*, 630(8016), pp. 493–500. doi: 10.1038/s41586-024-07487-w.

563 Bankhead, P. *et al.* (2017) 'QuPath: Open source software for digital pathology image analysis', *Scientific*
564 *Reports 2017 7:1*, 7(1), pp. 1–7. doi: 10.1038/s41598-017-17204-5.

565 Beales, P. L. *et al.* (1999) 'New criteria for improved diagnosis of Bardet-Biedl syndrome: results of a
566 population survey', *Journal of Medical Genetics*, 36(6), p. 437. doi: 10.1136/jmg.36.6.437.

567 Bentley-Ford, M. R. *et al.* (2021) 'A mouse model of BBS identifies developmental and homeostatic
568 effects of BBS5 mutation and identifies novel pituitary abnormalities', *Human molecular genetics*, 30(3–
569 4), pp. 234–246. doi: 10.1093/HMG/DDAB039.

570 Brücker, L. *et al.* (2023) 'The actin-bundling protein Fascin-1 modulates ciliary signalling', *Journal of*
571 *Molecular Cell Biology*, 15(4), p. 22. doi: 10.1093/JMCB/MJAD022.

572 Cao, Y. *et al.* (2009) 'Chemical modifier screen identifies HDAC inhibitors as suppressors of PKD models',
573 *Proceedings of the National Academy of Sciences of the United States of America*, 106(51), pp. 21819–
574 21824. doi: 10.1073/PNAS.0911987106.

575 Cognard, N. *et al.* (2015) 'Comparing the Bbs10 complete knockout phenotype with a specific renal
576 epithelial knockout one highlights the link between renal defects and systemic inactivation in mice', *Cilia*,
577 4. Available at: https://ciliajournal.biomedcentral.com/articles/10.1186/s13630-015-0019-8 (Accessed:
578 30 March 2021).

579 Dafinger, C. *et al.* (2021) 'Targeted deletion of Ruvbl1 results in severe defects of epidermal development
580 and perinatal mortality', *Molecular and Cellular Pediatrics*, 8(1). doi: 10.1186/S40348-021-00111-1.

581 Davis, R. E. *et al.* (2007) 'A knockin mouse model of the Bardet-Biedl syndrome 1 M390R mutation has
582 cilia defects, ventriculomegaly, retinopathy, and obesity', *Proceedings of the National Academy of*
583 *Sciences of the United States of America*, 104(49), pp. 19422–19427. doi: 10.1073/PNAS.0708571104.

584 Dilan, T. L. *et al.* (2018) 'Bardet-Biedl syndrome-8 (BBS8) protein is crucial for the development of outer
585 segments in photoreceptor neurons.', *Human molecular genetics*, 27(2), pp. 283–294. doi:
586 10.1093/hmg/ddx399.

587 Elawad, O. A. M. A. *et al.* (2022) 'Bardet–Biedl syndrome: a case series', *Journal of Medical Case Reports*,

588 16(1), pp. 1–9. doi: 10.1186/S13256-022-03396-6/FIGURES/4.

589 Endicott, S. J. and Brueckner, M. (2018) 'NUP98 Sets the Size-Exclusion Diffusion Limit through the Ciliary
590 Base', *Current biology: CB*, 28(10), pp. 1643-1650.e3. doi: 10.1016/J.CUB.2018.04.014.

591 Fan, C.-M. and Tessier-Lavigne, M. (1994) 'Patterning of mammalian somites by surface ectoderm and
592 notochord: Evidence for sclerotome induction by a hedgehog homolog', *Cell*, 79(7), pp. 1175–1186. doi:
593 10.1016/0092-8674(94)90009-4.

594 Fath, M. A. *et al.* (2005) 'Mkks-null mice have a phenotype resembling Bardet-Biedl syndrome', *Human*
595 *molecular genetics*, 14(9), pp. 1109–1118. doi: 10.1093/HMG/DDI123.

596 Forsythe, E. *et al.* (2017) 'Risk factors for severe renal disease in bardet-biedl syndrome', *Journal of the*
597 *American Society of Nephrology*, 28(3), pp. 963–970. doi: 10.1681/ASN.2015091029.

598 Forsythe, E. and Beales, P. L. (2013) 'Bardet–Biedl syndrome', *European Journal of Human Genetics*,
599 21(1), pp. 8–13. doi: 10.1038/ejhg.2012.115.

600 Garcia-Gonzalo, F. R. and Reiter, J. F. (2017) 'Open Sesame: How Transition Fibers and the Transition
601 Zone Control Ciliary Composition', *Cold Spring Harbor perspectives in biology*, 9(2). doi:
602 10.1101/CSHPERSPECT.A028134.

603 Gopalakrishnan, J. *et al.* (2023) 'Emerging principles of primary cilia dynamics in controlling tissue
604 organization and function', *The EMBO Journal*, p. e113891. doi: 10.15252/EMBJ.2023113891.

605 Guo, D. F. *et al.* (2011) 'Inactivation of Bardet-Biedl syndrome genes causes kidney defects', *American*
606 *Journal of Physiology - Renal Physiology*, 300(2), p. F574. doi: 10.1152/AJPRENAL.00150.2010.

607 Habbig, S. *et al.* (2011) 'NPHP4, a cilia-associated protein, negatively regulates the Hippo pathway', *The*
608 *Journal of cell biology*, 193(4), pp. 633–642. doi: 10.1083/JCB.201009069.

609 Hammarsjö, A. *et al.* (2021) 'High diagnostic yield in skeletal ciliopathies using massively parallel genome
610 sequencing, structural variant screening and RNA analyses', *Journal of Human Genetics 2021 66:10*,
611 66(10), pp. 995–1008. doi: 10.1038/s10038-021-00925-x.

612 Hildebrandt, F., Benzing, T. and Katsanis, N. (2011) 'Ciliopathies', *The New England journal of medicine*,
613 364(16), pp. 1533–1543. doi: 10.1056/NEJMRA1010172.

614 Hildebrandt, F. and Zhou, W. (2007) 'Nephronophthisis-associated ciliopathies.', *Journal of the American*
615 *Society of Nephrology: JASN*, 18(6), pp. 1855–71. doi: 10.1681/ASN.2006121344.

616 Ho, T. C. S., Chan, A. H. Y. and Ganesan, A. (2020) 'Thirty Years of HDAC Inhibitors: 2020 Insight and
617 Hindsight', *Journal of Medicinal Chemistry*, 63(21), pp. 12460–12484. doi:
618 10.1021/ACS.JMEDCHEM.0C00830/ASSET/IMAGES/LARGE/JM0C00830_0023.JPEG.

619 Jensen, V. L. *et al.* (2018) 'Role for intraflagellar transport in building a functional transition zone', *EMBO*
620 *reports*, 19(12). doi: 10.15252/EMBR.201845862.

621 Kobayashi, T. *et al.* (2017) 'HDAC2 promotes loss of primary cilia in pancreatic ductal adenocarcinoma',
622 *EMBO reports*, 18(2), pp. 334–343. doi: 10.15252/EMBR.201541922.

623 Kretschmer, V. *et al.* (2019) 'Progressive Characterization of Visual Phenotype in Bardet-Biedl Syndrome
624 Mutant Mice', *Investigative ophthalmology & visual science*, 60(4), pp. 1132–1143. doi: 10.1167/IOVS.18-
625 25210.

626 Kretschmer, V. *et al.* (2023) 'Deletion of IFT20 exclusively in the RPE ablates primary cilia and leads to
627 retinal degeneration', *PLoS biology*, 21(12). doi: 10.1371/JOURNAL.PBIO.3002402.

628 Kulaga, H. M. *et al.* (2004) 'Loss of BBS proteins causes anosmia in humans and defects in olfactory cilia
629 structure and function in the mouse', *Nature genetics*, 36(9), pp. 994–998. doi: 10.1038/NG1418.

630 Liu, W. *et al.* (2021) 'A Multi-Center, Real-World Study of Chidamide for Patients With Relapsed or
631 Refractory Peripheral T-Cell Lymphomas in China', *Frontiers in Oncology*, 11, p. 750323. doi:
632 10.3389/FONC.2021.750323/BIBTEX.

633 Loktev, A. V. *et al.* (2008) 'A BBSome Subunit Links Ciliogenesis, Microtubule Stability, and Acetylation',
634 *Developmental Cell*, 15(6), pp. 854–865. doi: 10.1016/j.devcel.2008.11.001.

635 May-Simera, H. L. *et al.* (2010) 'Bbs8, together with the planar cell polarity protein Vangl2, is required to
636 establish left-right asymmetry in zebrafish', *Developmental biology*, 345(2), pp. 215–225. doi:
637 10.1016/J.YDBIO.2010.07.013.

638 May-Simera, H. L. *et al.* (2015) 'Ciliary proteins Bbs8 and Ift20 promote planar cell polarity in the
639 cochlea', *Development (Cambridge, England)*, 142(3), pp. 555–566. doi: 10.1242/DEV.113696.

640 McConnachie, D. J., Stow, J. L. and Mallett, A. J. (2021) 'Ciliopathies and the Kidney: A Review', *American*
641 *journal of kidney diseases: the official journal of the National Kidney Foundation*, 77(3), pp. 410–419.
642 doi: 10.1053/J.AJKD.2020.08.012.

643 Meng, E. C. *et al.* (2023) 'UCSF ChimeraX: Tools for structure building and analysis', *Protein Science*,

644 32(11), p. e4792. doi: 10.1002/PRO.4792.

645 Monis, W. J., Faundez, V. and Pazour, G. J. (2017) 'BLOC-1 is required for selective membrane protein
646 trafficking from endosomes to primary cilia', *The Journal of cell biology*, 216(7), pp. 2131–2150. doi:
647 10.1083/JCB.201611138.

648 Munsterberg, A. E. *et al.* (1995) 'Combinatorial signaling by Sonic hedgehog and Wnt family members
649 induces myogenic bHLH gene expression in the somite.', *Genes & Development*, 9(23), pp. 2911–2922.
650 doi: 10.1101/gad.9.23.2911.

651 Mykytyn, K. *et al.* (2004) 'Bardet-Biedl syndrome type 4 (BBS4)-null mice implicate Bbs4 in flagella
652 formation but not global cilia assembly', *Proceedings of the National Academy of Sciences of the United*
653 *States of America*, 101(23), pp. 8664–8669. doi: 10.1073/PNAS.0402354101.

654 Nachury, M. V. *et al.* (2007) 'A Core Complex of BBS Proteins Cooperates with the GTPase Rab8 to
655 Promote Ciliary Membrane Biogenesis', *Cell*, 129(6), pp. 1201–1213. doi: 10.1016/j.cell.2007.03.053.

656 Nishimura, D. Y. *et al.* (2004) 'Bbs2-null mice have neurosensory deficits, a defect in social dominance,
657 and retinopathy associated with mislocalization of rhodopsin', *Proceedings of the National Academy of*
658 *Sciences of the United States of America*, 101(47), pp. 16588–16593. doi: 10.1073/PNAS.0405496101.

659 Patnaik, S. R. *et al.* (2019) 'Bardet–Biedl Syndrome proteins regulate cilia disassembly during tissue
660 maturation', *Cellular and Molecular Life Sciences*, 76(4), pp. 757–775. doi: 10.1007/s00018-018-2966-x.

661 Pazour, G. J. and Bloodgood, R. A. (2008) 'Targeting Proteins to the Ciliary Membrane', *Current Topics in*
662 *Developmental Biology*, 85, pp. 115–149. doi: 10.1016/S0070-2153(08)00805-3.

663 Pettersen, E. F. *et al.* (2021) 'UCSF ChimeraX: Structure visualization for researchers, educators, and
664 developers', *Protein science: a publication of the Protein Society*, 30(1), pp. 70–82. doi:
665 10.1002/PRO.3943.

666 Perez-Riverol, J. *et al.* (2024) 'The PRIDE database at 20 years: 2025 update', *Nucleic Acids Res*. doi:
667 10.1093/nar/gkae1011

668 Piceci-Sparascio, F. *et al.* (2023) 'Clinical variability in DYNC2H1-related skeletal ciliopathies includes Ellis-
669 van Creveld syndrome', *European Journal of Human Genetics 2023 31:4*, 31(4), pp. 479–484. doi:
670 10.1038/s41431-022-01276-7.

671 Postma, M. and Goedhartid, J. (2019) 'PlotsOfData-A web app for visualizing data together with their

672 summaries'. doi: 10.1371/journal.pbio.3000202.

673 Pourquié, O. *et al.* (1996) 'Lateral and Axial Signals Involved in Avian Somite Patterning: A Role for
674 BMP4', *Cell*, 84(3), pp. 461–471. doi: 10.1016/S0092-8674(00)81291-X.

675 Pugacheva, E. N. *et al.* (2007) 'HEF1-dependent Aurora A activation induces disassembly of the primary
676 cilium', *Cell*, 129(7), pp. 1351–1363. doi: 10.1016/J.CELL.2007.04.035.

677 Putoux, A. *et al.* (2012) 'Phenotypic variability of Bardet-Biedl syndrome: focusing on the kidney',
678 *Pediatric Nephrology*, 27(1), pp. 7–15. doi: 10.1007/s00467-010-1751-3.

679 Rahmouni, K. *et al.* (2008) 'Leptin resistance contributes to obesity and hypertension in mouse models of
680 Bardet-Biedl syndrome', *The Journal of clinical investigation*, 118(4), pp. 1458–1467. doi:
681 10.1172/JCI32357.

682 Reiter, J. F., Blacque, O. E. and Leroux, M. R. (2012) 'The base of the cilium: roles for transition fibres and
683 the transition zone in ciliary formation, maintenance and compartmentalization', *EMBO Reports*, 13(7),
684 p. 608. doi: 10.1038/EMBOR.2012.73.

685 Reiter, J. F. and Leroux, M. R. (2017) 'Genes and molecular pathways underpinning ciliopathies', *Nature*
686 *Reviews Molecular Cell Biology 2017 18:9*, 18(9), pp. 533–547. doi: 10.1038/nrm.2017.60.

687 Rödig, N. *et al.* (2022) 'Behavioral Phenotyping of Bbs6 and Bbs8 Knockout Mice Reveals Major
688 Alterations in Communication and Anxiety', *International Journal of Molecular Sciences*, 23(23). doi:
689 10.3390/IJMS232314506/S1.

690 Schindelin, J. *et al.* (2012) 'Fiji: an open-source platform for biological-image analysis', *Nature Methods*
691 *2012 9:7*, 9(7), pp. 676–682. doi: 10.1038/nmeth.2019.

692 Schneider, S. *et al.* (2021) 'Loss of Ciliary Gene Bbs8 Results in Physiological Defects in the Retinal
693 Pigment Epithelium', *Frontiers in Cell and Developmental Biology*, 9, p. 607121. doi:
694 10.3389/FCELL.2021.607121/FULL.

695 Seo, S. *et al.* (2009) 'Requirement of Bardet-Biedl syndrome proteins for leptin receptor signaling',
696 *Human molecular genetics*, 18(7), pp. 1323–1331. doi: 10.1093/HMG/DDP031.

697 Seo, S. *et al.* (2010) 'BBS6, BBS10, and BBS12 form a complex with CCT/TRiC family chaperonins and
698 mediate BBSome assembly.', *Proceedings of the National Academy of Sciences of the United States of*
699 *America*, 107(4), pp. 1488–93. doi: 10.1073/pnas.0910268107.

700 Sieckmann, K. *et al.* (2024) 'BBSome-dependent ciliary Hedgehog signaling governs cell fate in the white
701 adipose tissue', *bioRxiv*, p. 2024.01.25.576526. doi: 10.1101/2024.01.25.576526.

702 Tadenev, A. L. D. *et al.* (2011) 'Loss of Bardet-Biedl syndrome protein-8 (BBS8) perturbs olfactory
703 function, protein localization, and axon targeting', *Proceedings of the National Academy of Sciences of*
704 *the United States of America*, 108(25), pp. 10320–10325. doi: 10.1073/PNAS.1016531108.

705 Todaro, G. J. and Green, H. (1963) 'Quantitative studies of the growth of mouse embryo cells in culture
706 and their development into established lines', *The Journal of cell biology*, 17(2), pp. 299–313. doi:
707 10.1083/JCB.17.2.299.

708 Tyanova, S. *et al.* (2016) 'The Perseus computational platform for comprehensive analysis of
709 (prote)omics data', *Nature Methods 2016 13:9*, 13(9), pp. 731–740. doi: 10.1038/nmeth.3901.

710 Tyanova, S., Temu, T. and Cox, J. (2016) 'The MaxQuant computational platform for mass
711 spectrometry–based shotgun proteomics', *Nature Protocols*, 11. doi: 10.1038/nprot.2016.136.

712 Utsunomiya, A. *et al.* (2022) 'Oral histone deacetylase inhibitor tucidinostat (HBI-8000) in patients with
713 relapsed or refractory adult T-cell leukemia/lymphoma: Phase IIb results', *Cancer Science*, 113(8), pp.
714 2778–2787. doi: 10.1111/CAS.15431.

715 Vig, A. *et al.* (2020) 'DYNC2H1 hypomorphic or retina-predominant variants cause nonsyndromic retinal
716 degeneration', *Genetics in Medicine*, 22(12), p. 2041. doi: 10.1038/S41436-020-0915-1.

717 Xun, C. *et al.* (2018) 'Circulating RBP4 Increase and Its Diagnosis of Chronic Kidney Disease', *Annals of*
718 *clinical and laboratory science*, 48(2), pp. 205–207. Available at:
719 https://pubmed.ncbi.nlm.nih.gov/29678848/ (Accessed: 20 February 2024).

720 Zaucke, F. *et al.* (2010) 'Uromodulin is expressed in renal primary cilia and UMOD mutations result in
721 decreased ciliary uromodulin expression', *Human Molecular Genetics*, 19(10), p. 1985. doi:
722 10.1093/HMG/DDQ077.

723 Zhang, Q. *et al.* (2012) 'Intrinsic protein-protein interaction-mediated and chaperonin-assisted sequential
724 assembly of stable bardet-biedl syndrome protein complex, the BBSome.', *The Journal of biological*
725 *chemistry*, 287(24), pp. 20625–35. doi: 10.1074/jbc.M112.341487.

726

727

Acknowledgements:

We would like to express our sincere gratitude to Angelika Köser, Serena Greco-Torres, and Stefanie Keller for their exceptional technical assistance. We also deeply appreciate the outstanding support provided by the CECAD Imaging Facility and the CECAD Proteomics Facility. Our heartfelt thanks go to all members of our research group. Lastly, we extend our appreciation to the patient and their advocate for their generous contributions and commitment to advancing research. We would also like to thank Edward Seto for kindly providing us with the HDAC2 Plasmid. Molecular graphics and analyses were performed with UCSF ChimeraX, developed by the Resource for Biocomputing, Visualization, and Informatics at the University of California, San Francisco, with support from National Institutes of Health R01-GM129325 and the Office of Cyber Infrastructure and Computational Biology, National Institute of Allergy and Infectious Diseases (Meng *et al.*, 2023). Funding: This study was supported by the German Research Foundation (DFG; SFB1403, project number 414786233, A09 to B.S. and T.B.; and FOR5547 to HMS, DW, and BS, project number 503306912, under Germany's Excellence Strategy – EXC2151 – Project-ID 390873048 (to D.W.), and WA 3382/8-1 – Project-ID 513767027 (to D.W.). The NEOCYST consortium (Network for Early Onset Cystic Kidney Diseases) supported the project, with funding provided by the German Ministry of Education and Research (BMBF) under grant agreement number 01GM1515D. This funding (to B.S., M.C.L. and M.C.) had no impact on the selection of the topic or the content of the position paper. B.S. and M.C.L.. were also supported by the European Union (TheraCil). P.M. was supported by the Studienstiftung des Deutschen Volkes. The CECAD proteomics facility was supported by the large instrument grant INST 1856/71-1 FUGG by the German Research Foundation (DFG Großgeräteantrag).

Author contributions:

EK, HMS and BS designed the study. EK and JG performed most of the experiments. PAM prepared the experiments for MEFs. LKE performed and analysed the BBS8 interactome MS/MS experiments. HMS, CK, DW, MC, MCL, TB provided materials and support for the interpretation of results. EK assembled the final figures. EK and BS wrote the original draft. All of the authors discussed the project and contributed to the final version of the manuscript.

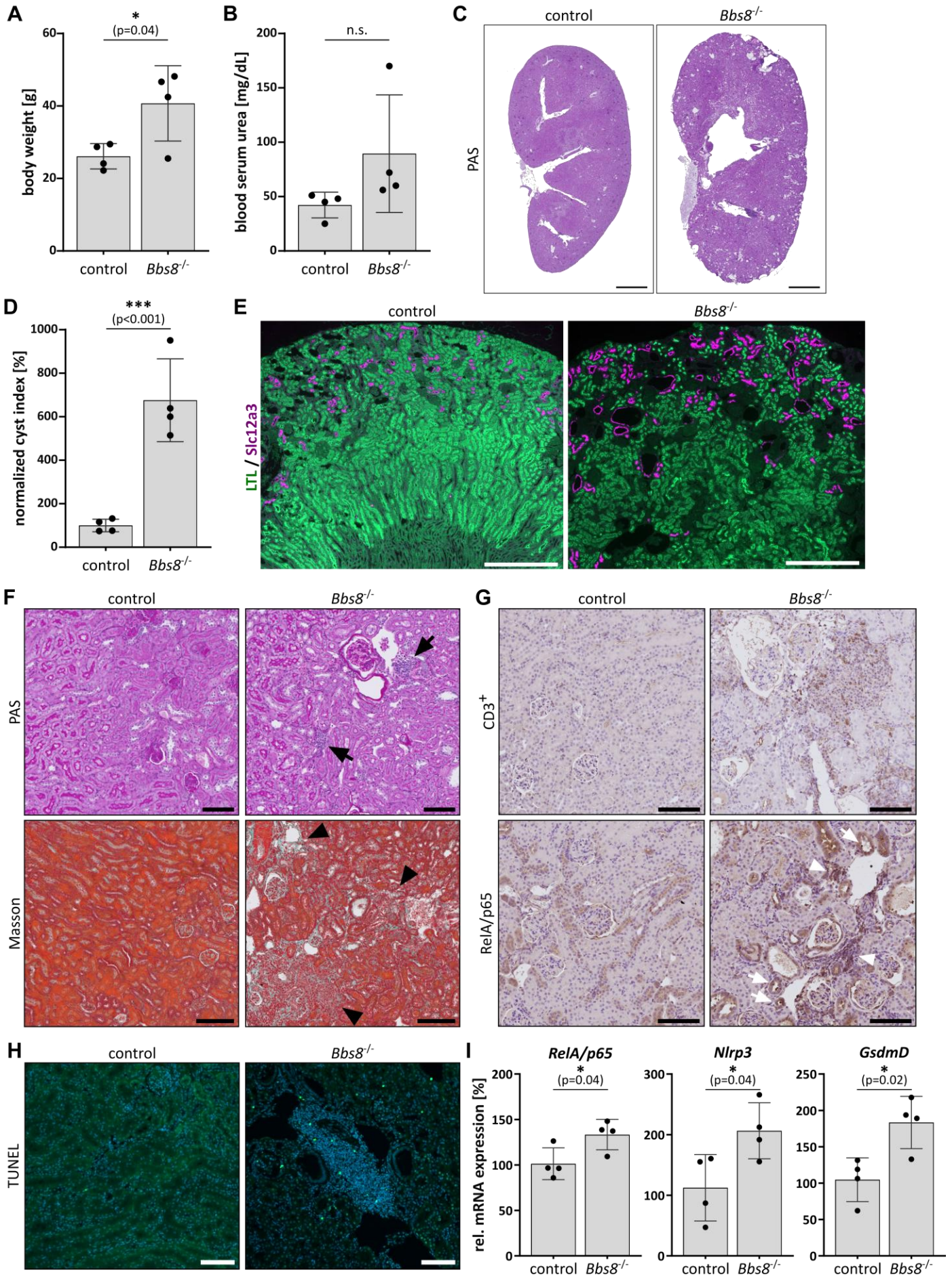
A
*
(p=0.04)
body weight [g]
control
Bbs8-/-
B
n.s.
blood serum urea [mg/dL]
control
Bbs8-/-
C
control
Bbs8-/-
PAS
D
***
(p<0.001)
normalized cyst index [%]
control
Bbs8-/-
E
control
Bbs8-/-
LTL / Slc12a3
F
control
Bbs8-/-
PAS
Masson
G
control
Bbs8-/-
CD3+
RelA/p65
H
control
Bbs8-/-
TUNEL
I
RelA/p65
*
(p=0.04)
Nlrp3
*
(p=0.04)
GsdmD
*
(p=0.02)
rel. mRNA expression [%]
control
Bbs8-/-

Figure 1

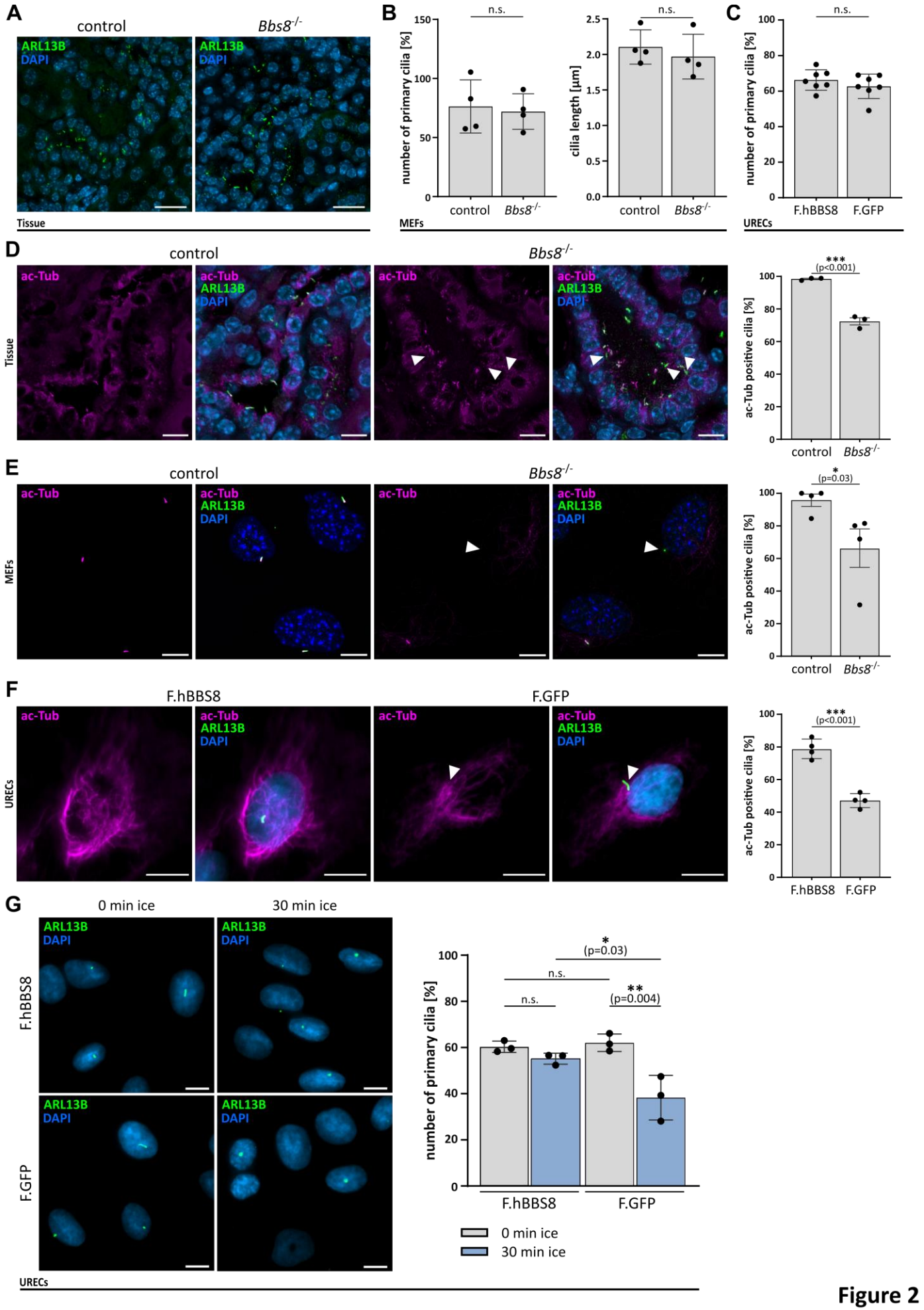
A
control
Bbs8-/-
ARL13B
DAPI
Tissue
B
n.s.
number of primary cilia [%]
cilia length [µm]
control
Bbs8-/-
MEFs
C
n.s.
number of primary cilia [%]
F.hBBS8
F.GFP
URECs
D
control
Bbs8-/-
ac-Tub
ARL13B
DAPI
Tissue
***
(p<0.001)
ac-Tub positive cilia [%]
E
*
(p=0.03)
MEFs
F
F.hBBS8
F.GFP
URECs
G
0 min ice
30 min ice
F.hBBS8
F.GFP
n.s.
**
(p=0.004)
0 min ice
30 min ice
URECs

Figure 2

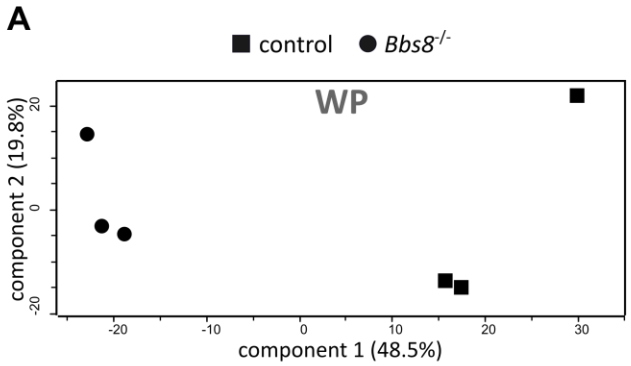

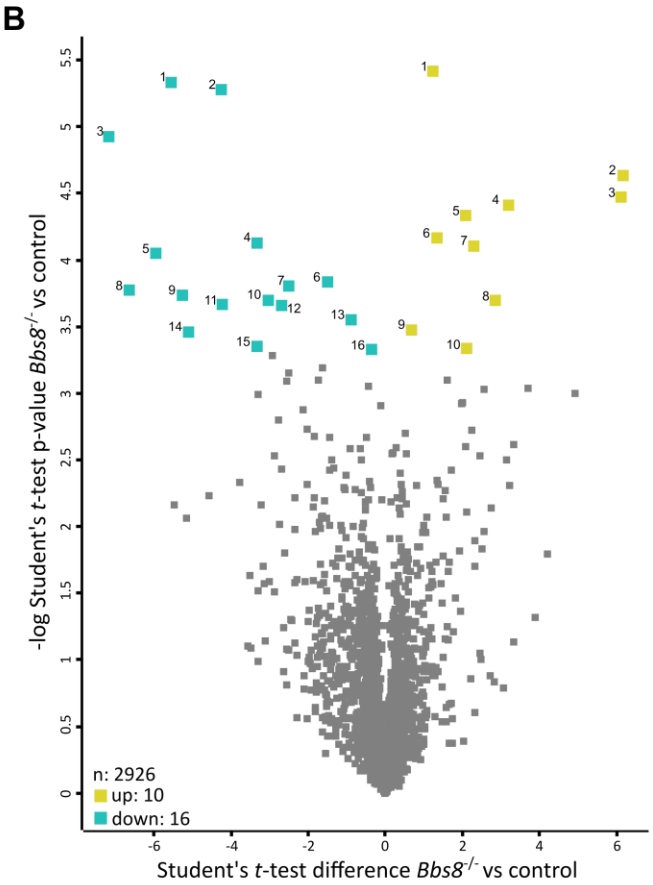

C

Up-Rregulated (-log p-value)			Down-Regulated (-log p-value)		
1	DCTN6	(5.41)	1	RBM22	(5.33)
2	THOC7	(4.63)	2	APOC1	(5.28)
3	AGO2	(4.47)	3	LYRM5	(4.92)
4	TTN	(4.41)	4	ACNAT2	(4.13)
5	HDAC2	(4.33)	5	GAR1	(4.05)
6	PARP3	(4.16)	6	ARHGAP18	(3.84)
7	NUP98	(4.10)	7	MRPL47	(3.80)
8	COPZ2	(3.70)	8	SYNE1	(3.77)
9	RBP4	(3.47)	9	DYNC2H1	(3.73)
10	UMOD	(3.33)	10	DAP	(3.70)
			11	UBE2V2	(3.67)
			12	NAA15	(3.66)
			13	ASPSCR1	(3.55)
			14	SUMO2	(3.46)
			15	DTNBP1	(3.35)
			16	MTHFD1	(3.33)

Tissue

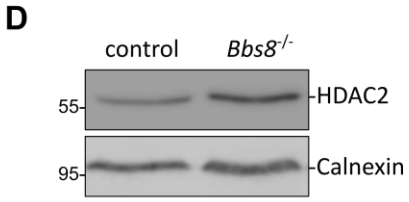

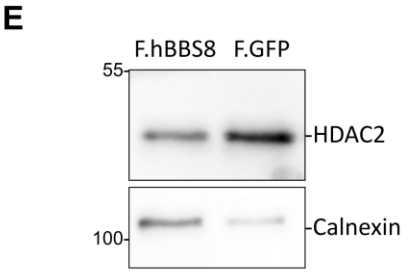

MEFs **URECs**

Figure 3

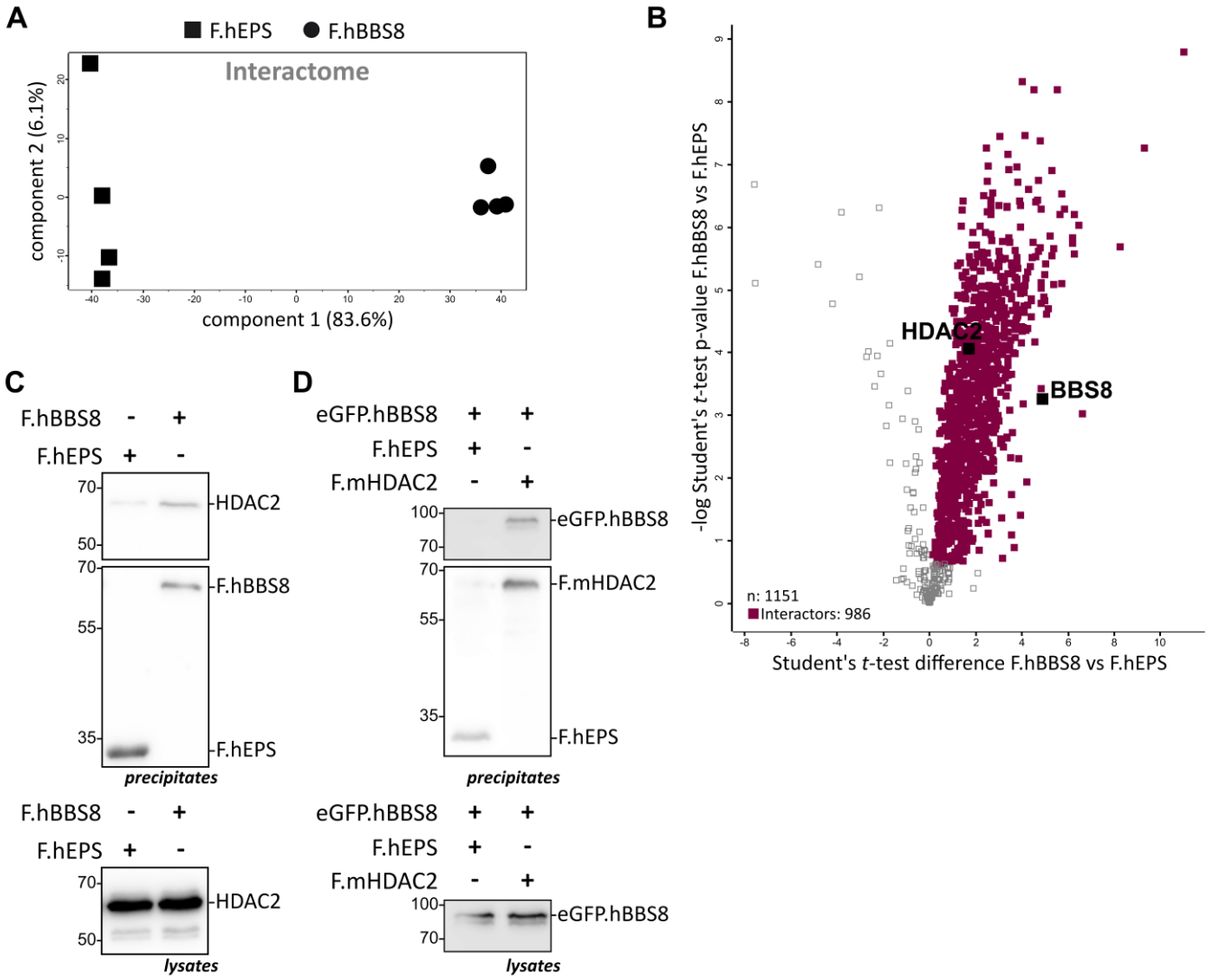
A
F.hEPS
F.hBBS8
Interactome
component 2 (6.1%)
component 1 (83.6%)
B
HDAC2
BBS8
n: 1151
Interactors: 986
-log Student's t-test p-value F.hBBS8 vs F.hEPS
Student's t-test difference F.hBBS8 vs F.hEPS
C
F.hBBS8
F.hEPS
HDAC2
F.hBBS8
F.hEPS
precipitates
lysates
D
eGFP.hBBS8
F.hEPS
F.mHDAC2
eGFP.hBBS8
F.mHDAC2
F.hEPS
precipitates
lysates

Figure 4

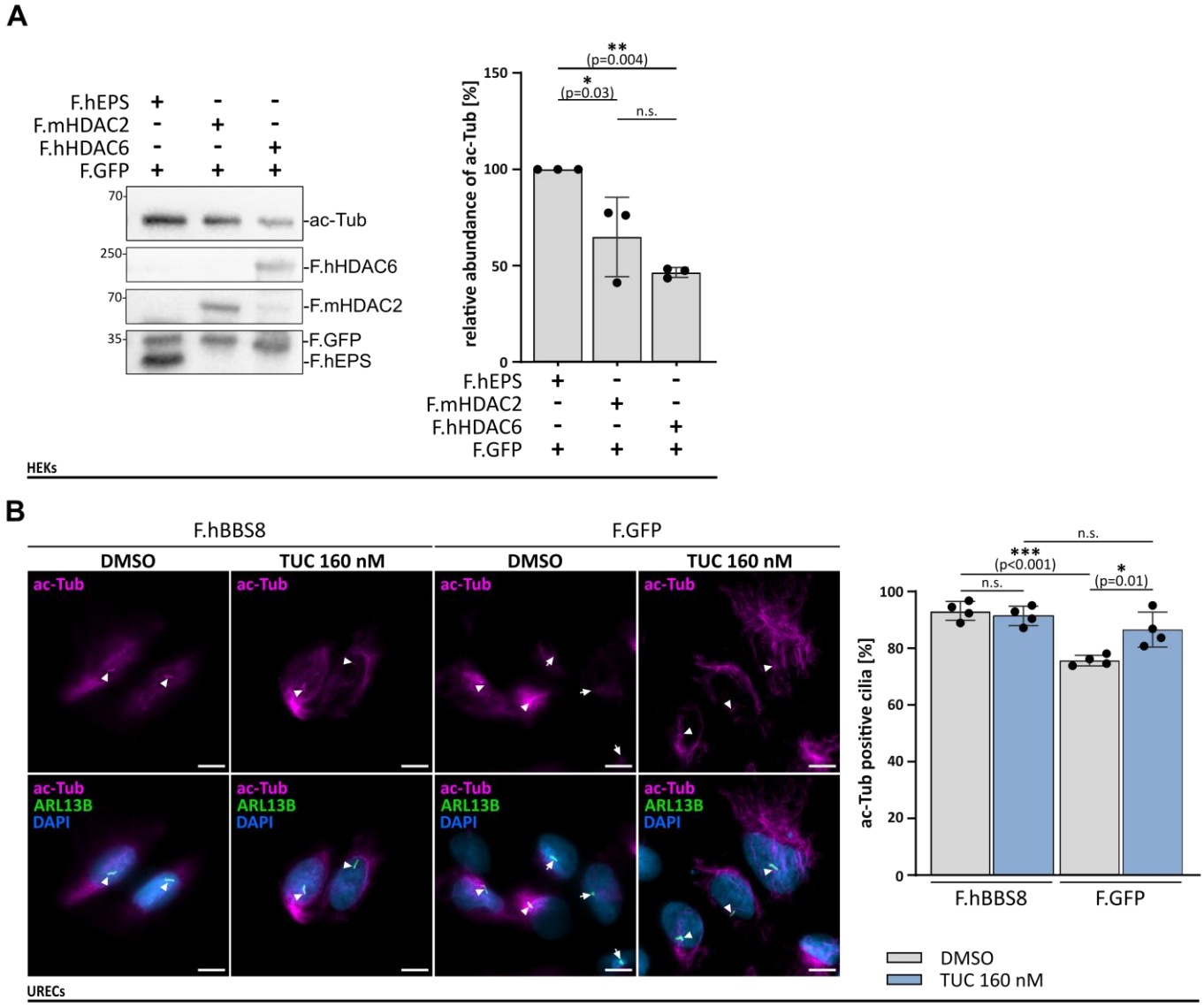
A
F.hEPS + - -
F.mHDAC2 - + -
F.hHDAC6 - - +
F.GFP + + +
70
250
70
35
ac-Tub
F.hHDAC6
F.mHDAC2
F.GFP
F.hEPS
relative abundance of ac-Tub [%]
150
100
50
0
**
(p=0.004)
*
(p=0.03)
n.s.
HEKs
B
F.hBBS8
F.GFP
DMSO
TUC 160 nM
ac-Tub
ac-Tub
ARL13B
DAPI
ac-Tub positive cilia [%]
100
80
60
40
20
0
***
(p<0.001)
n.s.
n.s.
*
(p=0.01)
F.hBBS8
F.GFP
DMSO
TUC 160 nM
URECs

Figure 5

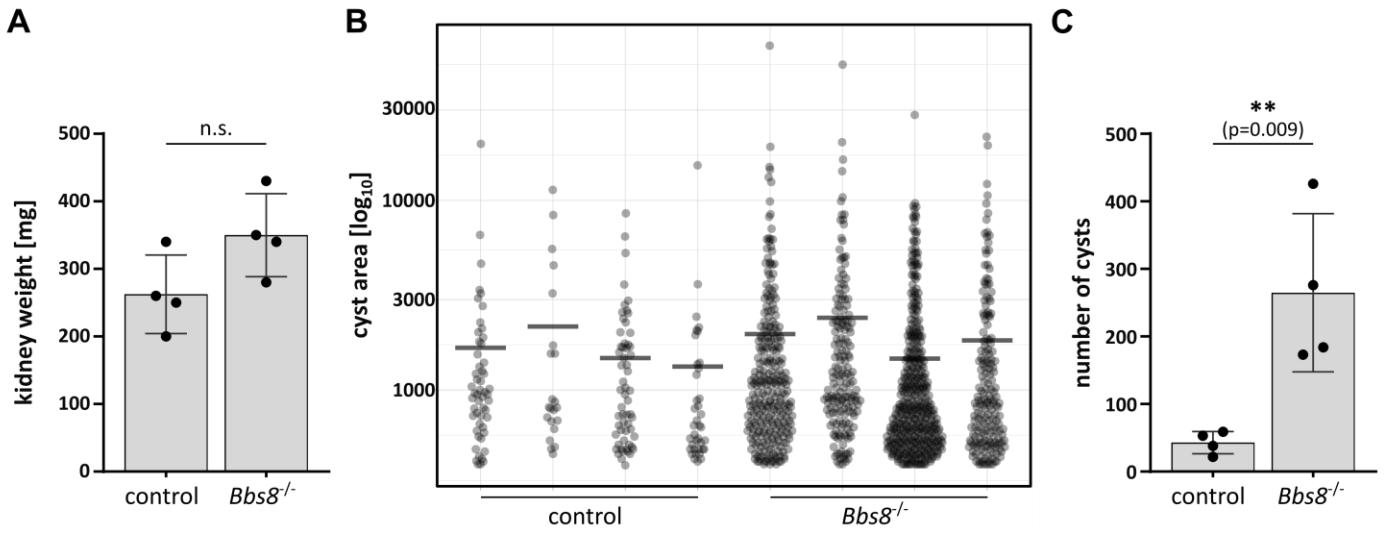

Supp. Figure 1

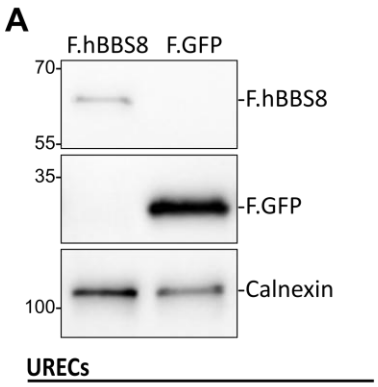

Supp. Figure 2

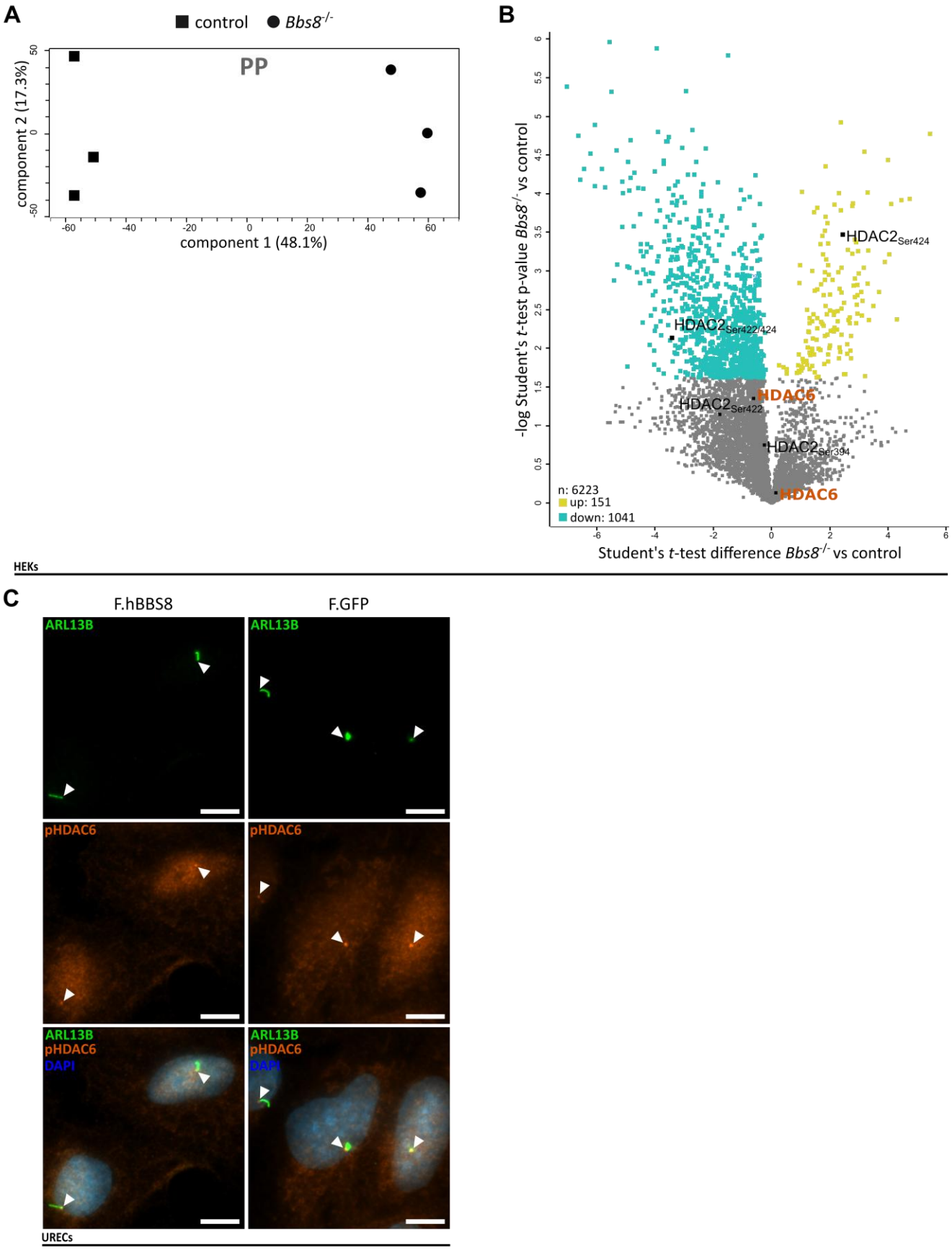

Supp. Figure 3

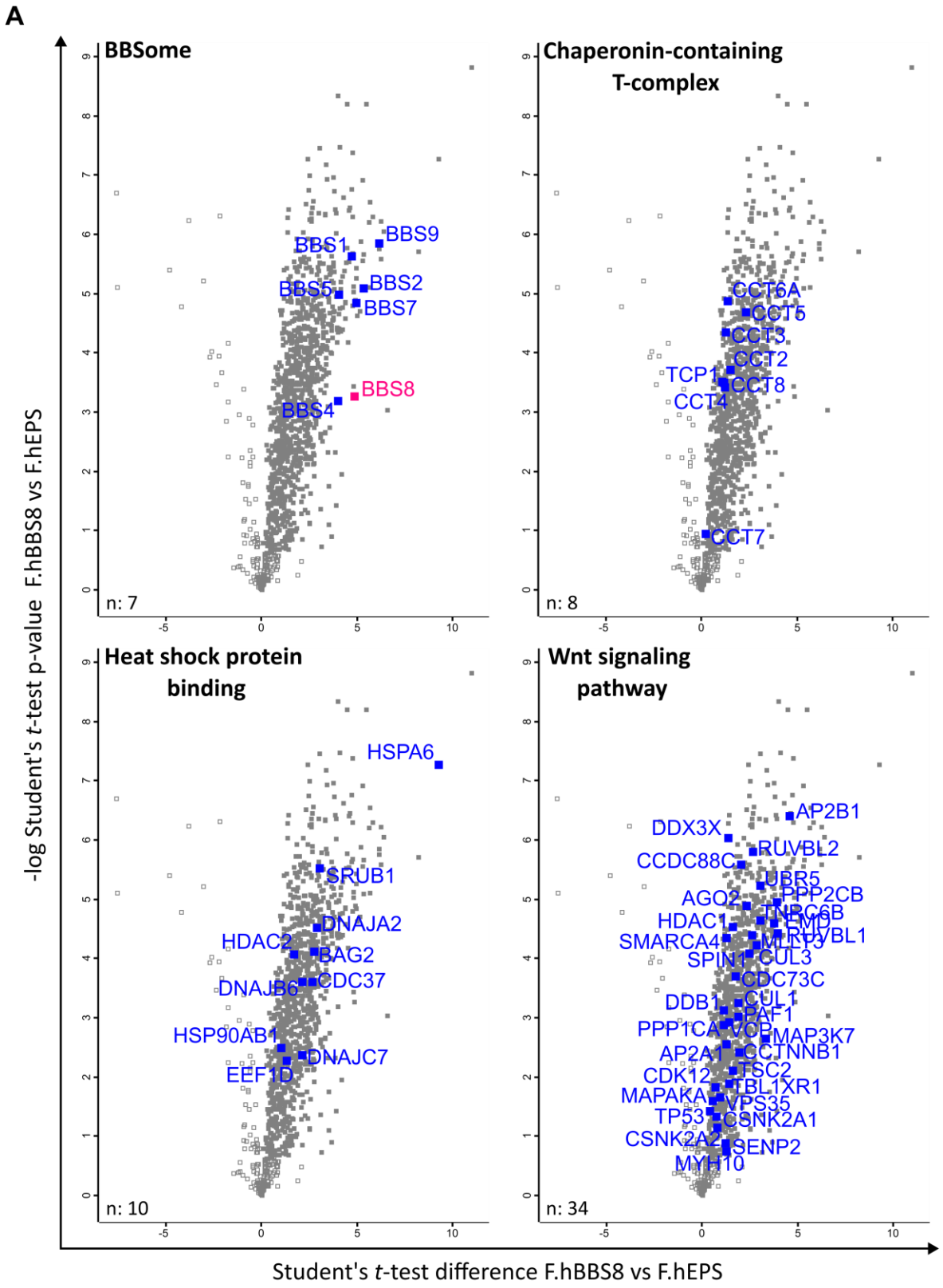

Supp. Figure 4

A

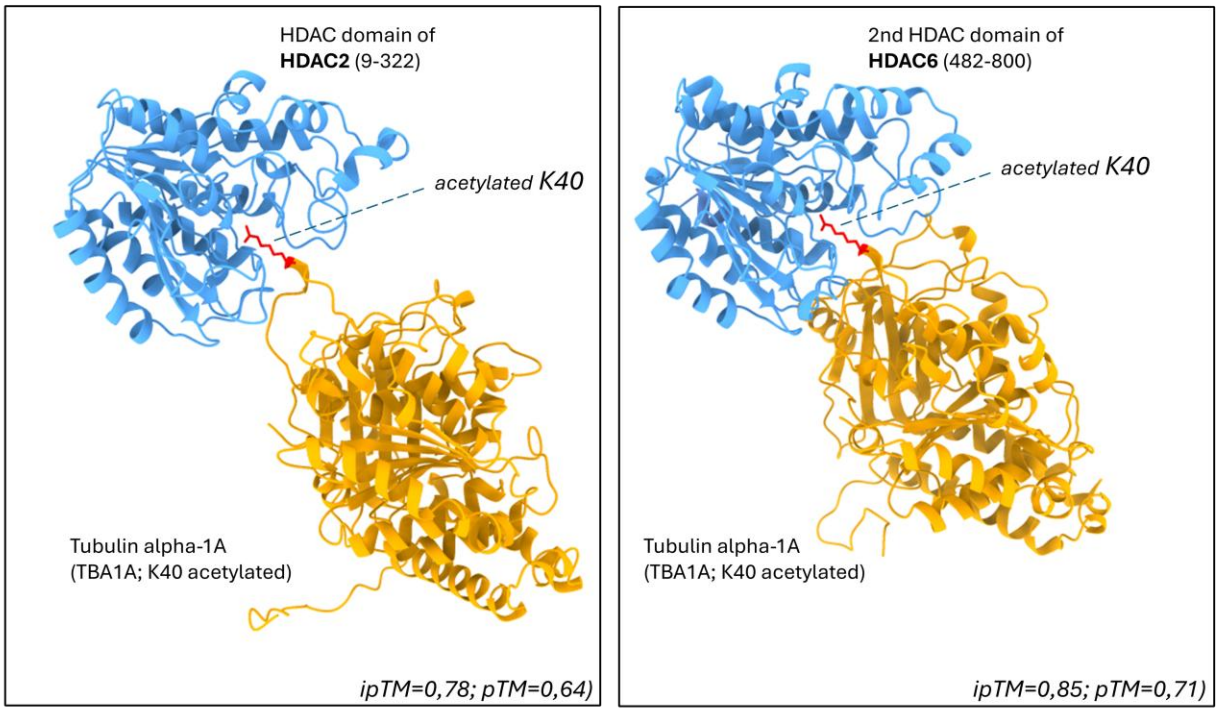

Supp. Figure 5

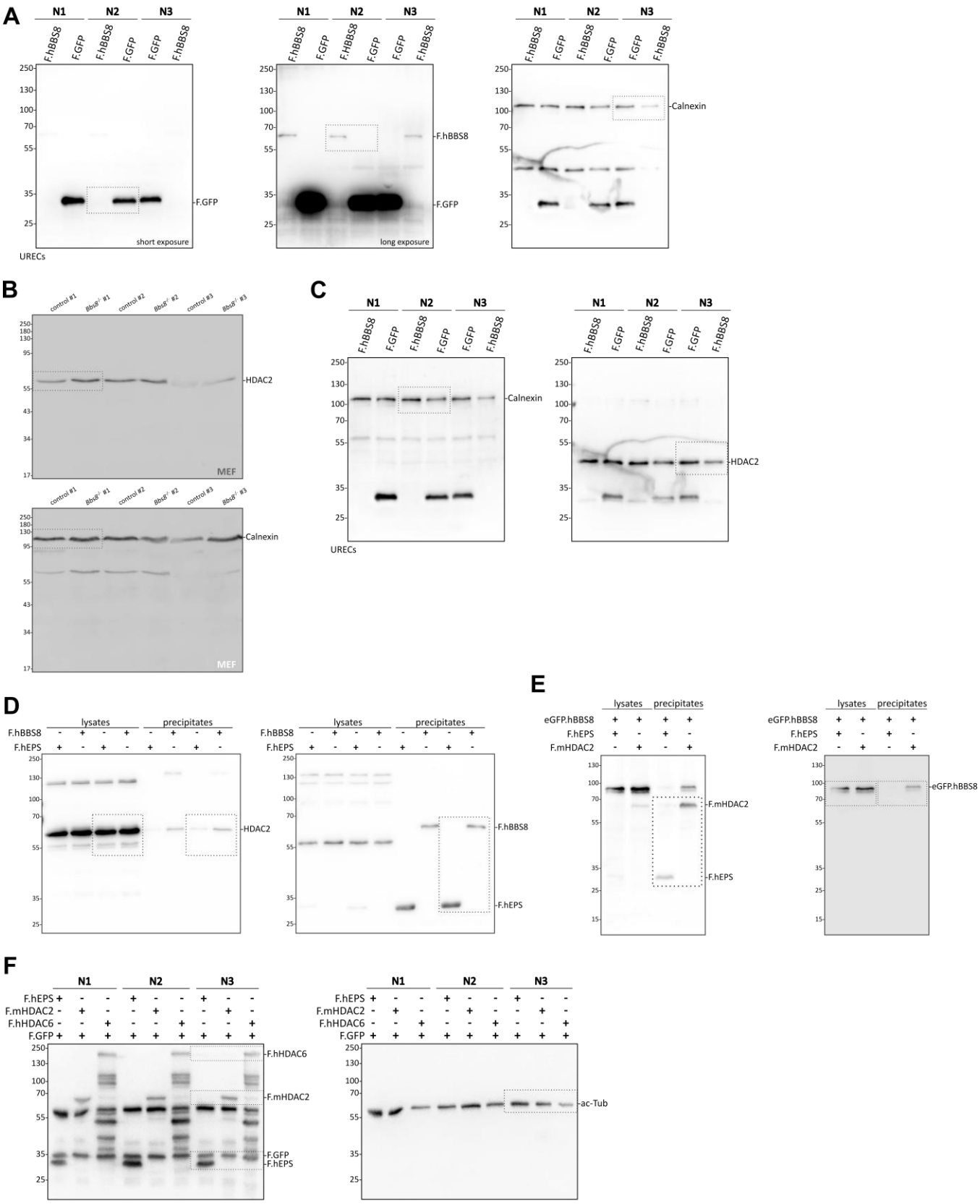

Supp. Figure 6